A SATELLITE-AUGMENTED ACOUSTIC SURVEILLANCE SYSTEM FOR THE CANADIAN ARCTIC

UN SYSTÈME DE SURVEILLANCE ACOUSTIQUE POUR L'ARCTIQUE CANADIEN AUGMENTÉE PAR SATELLITE

A Thesis Submitted to the Division of Graduate Studies
of the Royal Military College of Canada
by

Stefan C. Tarla, BScH

In Partial Fulfillment of the Requirements for the Degree of
Master of Science in Physics

January 2023

To Germinia and Cristian

Acknowledgements

I would first like to extend my gratitude to my supervisor, Dr. Ron Vincent whose guidance and mentorship has been integral to the success of this research and to my success and professional development as a researcher. I'd also like to thank Dr. Kathryn McWilliams, Dr. Ron Vincent, and Dr. L Sangalli for coordinating the NSERC CREATE International Space Mission Training Program, which has both funded my research and enabled me to meet and collaborate with many wonderful students from across the country. Finally, I would like to thank my parents for their undying support in all of my endeavours. None of this would have been possible without them.

Abstract

The melting of Arctic sea ice is making the Canadian Arctic more navigable to surface and sub-surface vessels already capable of navigating this harsh environment. In the post-Cold War world order, Canada can no longer solely rely on the United States to protect the Arctic. The limited equipment and man power of the modern Canadian Armed Forces does not allow for consistent situational awareness of the Arctic region. An increasingly accessible Arctic is of great interest to many foreign countries looking to take advantage of untapped natural resources and alternative shipping lanes. This presents a pressing national security concern for Canada.

As part of the new NORAD modernization program, a satellite-augmented acoustic surveillance system would provide continuous monitoring of the waters of the Canadian Arctic Archipelago. Hydrophones placed in strategic locations in and around the Canadian Arctic Archipelago provide continuous acoustic monitoring for surface and sub-surface contacts. A constellation of low Earth orbit satellites capable of providing 100% daily coverage of the region acts as a data relay system receiving acoustic signals of interest from the hydrophones and downlinking the data to ground stations at defence installations in Halifax, Winnipeg, and Victoria.

Significant interest in this concept has allowed for the development of the Audimus mission, a satellite mission led by the Royal Military College of Canada sponsored by Defence Research and Development Canada as part of the Canadian Space Agency CubeSats Initiative in Canada for STEM. This mission seeks to demonstrate the feasibility of transmitting acoustic data from a hydrophone to a satellite. Mission success will serve as an important step towards the full implementation of the proposed system.

Résumé

La fonte de la glace de mer arctique rend l'Arctique Canadien plus navigable
pour les navires de surface et sous-marins déjà capables de naviguer dans cet
environnement hostile. Dans l'ordre mondial post-Guerre Froide, le Canada
ne peut plus compter uniquement sur les États-Unis pour protéger l'Arctique.
L'équipement et la main-d'œuvre limités des Forces Armées Canadiennes mod-
ernes ne permettent pas une prise de conscience de la situation de la région
Arctique de manière cohérente. Un Arctique de plus en plus accessible suscite
un grand intérêt pour de nombreux pays étrangers cherchant à profiter des
ressources naturelles inexploitées et des voies de navigation alternatives. Cela
présente une préoccupation de sécurité nationale pressante pour le Canada.

Dans le cadre du nouveau programme de modernisation de NORAD,
un système de surveillance acoustique augmenté par satellite fournirait une
surveillance continue des eaux de l'Archipel Arctique Canadien. Des hy-
drophones placées dans des emplacements stratégiques dans et autour de
l'Archipel Arctique Canadien assurent une surveillance acoustique continue
des contacts de surface et sous-surface. Une constellation de satellites en or-
bite terrestre basse, capable de fournir une couverture quotidienne à 100% de
la région, agit comme un système de relais de données recevant les signaux
acoustiques d'intérêt des hydrophones et téléchargeant les données vers les
stations terrestres des installations de défense à Halifax, Winnipeg et Victo-
ria.

L'intérêt significatif pour ce concept a permis le développement de la mis-
sion Audimus, une mission satellitaire dirigée par le Collège Militaire Royal du
Canada et parrainée par Recherche et Développement pour la Défense Canada
dans le cadre de l'initiative CubeSats de l'Agence Spatiale Canadienne pour
les STEM. Cette mission vise à démontrer la faisabilité de la transmission de
données acoustiques d'une hydrophone à un satellite. Le succès de la mission
constituera une étape importante vers la mise en œuvre complète du système
proposé

Contents

List of Tables

List of Figures

List of Acronyms and Abbreviations

ADCS	Attitude Determination and Control System
BOL	Beginning of Life
CAA	Canadian Arctic Archipelago
CFB	Canadian Forces Base
COTS	Commercial Off-The-Shelf
CUBICS	Canadian Space Agency CubeSats Initiative in Canada for STEM
DIFAR	Directional Frequency Analysis and Recording
DOD	Depth of Discharge
DORIS	Doppler Orbitography and Radio-positioning Integrated by Satellite
EEZ	Exclusive Economic Zone
EIRP	Effective Isotropic Radiated Power
EOL	End of Life
GEO	Geostationary Orbit
GNSS	Global Navigation Satellite System
IGSO	Inclined Geosynchronous Orbit
HLA	Horizontal Line Array
IR	Infrared
LEO	Lower Earth Orbit
LOFAR	Low Frequency Analysis and Recording
MEO	Medium Earth Orbit
NORAD	North American Aerospace Defence Command
PML	Polar Mixed Layer
PSU	Practical Salinity Units
RAAN	Right Ascension of the Ascending Node
RMC	Royal Military College of Canada
SOFAR	Sound Fixing and Ranging Channel

STK	Systems Tool Kit
TLE	Two-Line Element Set
TT&C	Telemetry, Tracking, and Command
UNCLOS	United Nations Convention on the Law of the Sea
VLA	Vertical Line Array

1 Introduction

1.1 Understanding Canadian Arctic Sovereignty and Security

Canadian sovereignty and security in the Arctic is facing an increasing number of challenges as a result of the melting of Arctic sea ice. Sovereignty is comprised of three elements. There must be a specifically defined territory, a people living within that territory, and a governance system that controls the territory [1]. The issue of defined boundaries is of greatest relevance to the discussion of Canadian sovereignty in the Arctic. The 1996 United Nations Convention on the Law of the Sea (UNCLOS) created new maritime zones and formally codified international law. Generally, the level of control the state can impose on a maritime zone decreases the further away that zone is from its shores [2]. The Exclusive Economic Zone (EEZ) extends 200 nautical miles from the shore and the state has control over all living and non-living resources within it. This means that the state has exclusive access to any resource exploitation in this zone and is the only entity that can grant permission to a foreign party to engage in resource exploitation in the area but it cannot control international shipping that is not exploiting resources [2]. A third zone that UNCLOS defines is a continental shelf zone where a state can claim control over all activities related to the seabed for another 150 nautical miles beyond the EEZ. This is taken to mean any development of oil and gas facilities but the state has no control over activities above the seabed in this area such as shipping or fishing [2]. The last zone that is of significance to the Canadian Arctic concerns a body of water that connects two international bodies of water and has been used for international shipping. This body is considered by UNCLOS to be within control of the state with the exception of international shipping [3]. Countries such as the United States, the European Union, Denmark, Japan, Russia, and Norway have challenged Canada's claim that the Northwest Passage falls within its internal waters and instead claim

that it should be considered an international strait as it connects the Atlantic and Pacific Oceans [4]. Given such a large number of Canada's allies dispute its claim over the Northwest Passage, a more independent approach must be taken toward securing this region.

The proliferation of nuclear weapons fundamentally changed the nature of security. Previously, a state's security was achieved by the ability to defend itself militarily or impose its will on another state [5]. States that were not powerful enough to act alone formed alliances with the aim of optimizing their economic capabilities to build militaries [5]. As nuclear weapons became more common, the ultimate goal of security shifted from the ability to win wars to the ability to deter hostile actors with the threat of nuclear war [6]. During this time, the concept of Arctic security was aligned with defence against aggression from the Soviet Union which was largely left to the United States [3]. As the Cold War came to an end, the Canadian government scrapped plans presented in the 1987 White Paper on Defence to purchase between 10 and 12 nuclear submarines and Polar Class 8 icebreakers capable of patrolling the Arctic year-round [7]. As a result, Canada's current strategic capabilities in the Arctic include a fleet of five icebreakers operated by the Canadian Coast Guard, the Canadian Forces Northern Area headquarters in Yellowknife, Northwest Territories, and the North American Aerospace Defence Command (NORAD) within which Canada maintains the North Warning System, an unmanned chain of radar sites for aerospace surveillance [4].The Royal Canadian Navy's new Harry DeWolf class Arctic offshore patrol vessel, primarily designed as a domestic constabulary vessel, is not well-equipped for an Arctic surveillance and defence mission given its lack of sub-surface monitoring capabilities, anti-submarine weaponry, and heavy anti-ship ordinance [8, 9]. As the Arctic environment continues to change at an accelerated rate, these capabilities are no longer sufficient to monitor Canada's northern territory.

1.2   Effects of Climate Change in the Arctic

The significant rise in the amount of carbon dioxide in the atmosphere, along with increases in the levels of methane and other airborne pollutants, is contributing to an increasingly pronounced greenhouse effect that is trapping heat inside the atmosphere. The Arctic is more severely impacted by the greenhouse effect. This phenomenon is known as Arctic Amplification and refers to the increased vulnerability of the Arctic to changes in the climate of the Earth due to its position and its environmental characteristics. The most compelling evidence for Arctic amplification exists in the form of the measured rise in av-

erage air temperatures in the Arctic over the past five decades. Over a 46-year period from 1971 to 2017, the average annual air temperature in the Arctic increased by 2.7°C which is approximately 2.4 times the average warming rate of the Northern Hemisphere [10].

As a result, the extent of Arctic Ocean sea ice has declined by over 50% since 1979 with the minimum extent of 3.39 million km occurring in 2012 as shown in Figure 1.1 [11, 12]. This has made transits under the ice easier for the nuclear submarines of today which are quieter, have more advanced weapons systems, and can stay submerged for longer than the first nuclear submarines capable of conducting transits under the Arctic ice starting in 1958 [13].
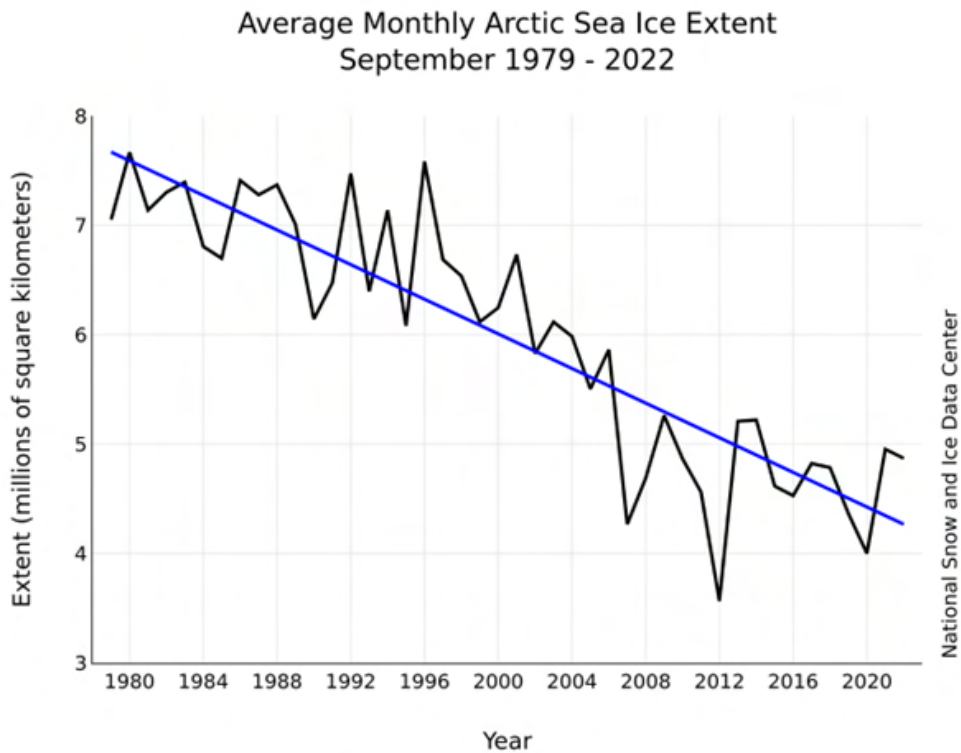
Figure 1.1: Time series of yearly minimum sea ice extent from the beginning of consistent satellite observations of the Arctic in 1979 to 2022 [14].

The concentration of carbon dioxide in the atmosphere remained relatively constant from the end of the Last Glacial Maximum to the middle of the 18$^{\text{th}}$

century when the industrial revolution began. Since the widespread implementation of internal combustion and fossil fuels into global industry and the everyday lives of the ever-increasing human population, the concentration of atmospheric carbon dioxide has increased from approximately 280 ppm to 420 ppm [15]. Figure 1.2 illustrates the increase in atmospheric carbon dioxide concentration.
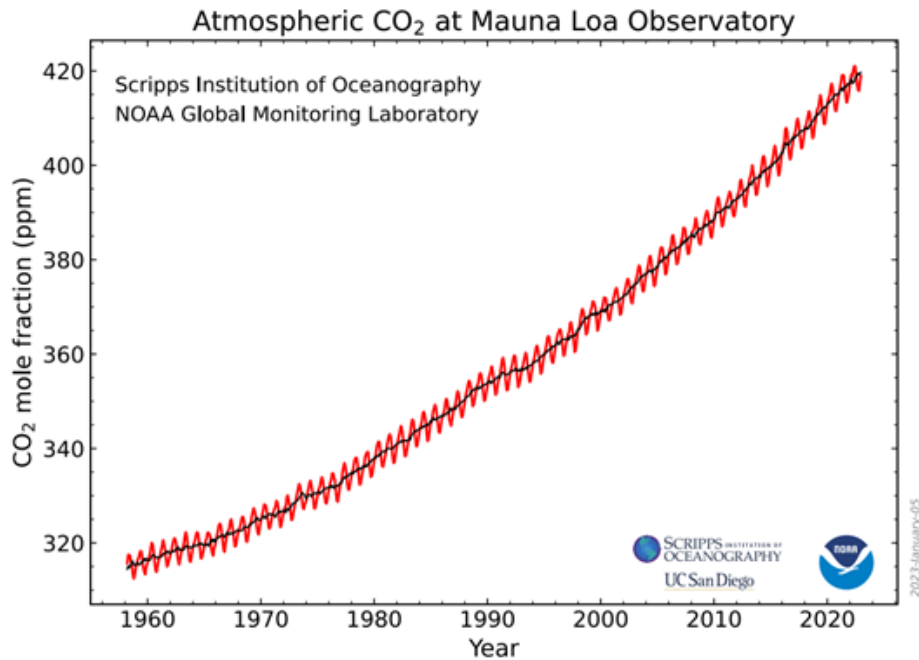
Figure 1.2: Monthly mean carbon dioxide concentration at Mauna Loa, Hawaii. The red line tracks monthly mean values centered around the middle of each month while the black line represents the same values after being corrected for the average seasonal cycle [16].

Arctic amplification occurs as a result of multiple feedback loops that are unique to the Arctic environment. The most significant feedback mechanism that contributes to the warming of the arctic is the reduction in year-round snow and ice coverage [17]. Snow and sea ice are highly reflective surfaces with albedos greater than 0.6 and redirect a large portion of the solar radiation that

4

strikes the areas they cover back out of the atmosphere [18]. As more snow and ice melts however, more dark surfaces such as the permafrost earth of the high tundra and the Arctic Ocean surface are exposed. These areas are characterized by extremely low albedos of less than 0.1 and therefore absorb more solar radiation which contributes to the increase of the global average temperature [18]. The loss of polar sea ice is a problem of increasing urgency as the rate of sea ice loss is increasing [11]. Between the start of satellite observations of sea ice coverage in the Arctic in the late 1970s to the end of the 1990s, the average decline in sea ice area was 3% per decade. When factoring in the following decade until 2008, the average rate of sea ice area decline rises to 10.7% per decade [11]. Another threat to the Arctic is the release of large amounts of carbon dioxide and methane into the atmosphere as a result of the thawing of the Arctic permafrost. The Arctic holds a large amount of carbon and methane under the permafrost in the form of organic biomass and natural gas deposits. As the climate warms, the permafrost thaws, and the trapped organic biomass begins to degrade, releasing carbon and methane into the atmosphere [19]. At numerous measurement sites throughout the Alaskan permafrost, the average temperature at 20 m below the surface was found to have increased by 2.5°C since 1972 [10]. There is between 1.4 and 1.6 trillion tons of carbon trapped in the Arctic permafrost and it is estimated that it is being released at a rate of 600 million tons per year [20]. A final feedback loop that must be taken into consideration when discussing the causes of Arctic amplification is the increased capacity of warmer air to retain moisture. As the air over the Arctic continues to warm, the capacity for retaining water vapor, the most abundant greenhouse gas in the atmosphere, increases. This in itself will intensify the warming effect and lead to further acceleration of Arctic warming [21].

1.3 Arctic Sea Ice Export

Another significant contributing mechanism to sea ice loss in the Arctic is sea ice export through three main waterways. These are Fram Strait, Nares Strait, and the Canadian Arctic Archipelago (CAA). Fram Strait sees the highest volume of Arctic sea ice export with the average annual amount totaling 883,000 km^2 with a range between 600,000 and 1.2 million km^2 from 1935-2014 [22]. The sea ice exported through Fram Strait is predominately thinner, annual sea ice which differs from the sea ice exported through Nares Strait and the CAA. In the 2017- 2018 season however, Fram Strait saw an approximately 50% reduction in the amount of sea ice exported due to the

reduction in overall Arctic sea ice extent [23].

Nares Strait is characterized by the formation of a northern ice arch that blocks sea ice from traversing its waters for multiple months. Recently, this ice arch has failed to form on multiple occasions. The years 2007, 2009, 2010, 2017, and 2019 saw no ice arch formation and consequently, a higher amount of Arctic sea ice export [24]. Nares Strait sees mostly thick, multi-year ice travelling southward from the Last Ice Area, a 2,000 km arc spanning from the western CAA to the north coast of Greenland [25]. Due to its reduced width and depth, the amount of ice that traverses this waterway regardless of ice arch formation is significantly smaller than Fram Strait. Over the period of 1997-2009, the average amount of annual sea ice export was approximately 42,000 km^2 , however, over a shorter period between 2017 and 2019 where the ice arch failed to consolidate for two of those years, the average rose to 86,000 km^2 [24].

The CAA differs greatly from both Fram Strait and Nares Strait due to its geography that includes many islands and small waterways. Like Nares Strait, the CAA is experiencing significant increases to its annual sea ice export volume. During the period of 1997 to 2018, the annual Arctic sea ice export through the CAA was 23,000 km^2 but, due to the decreasing proportion of thick, multi-year ice, fewer blockages of the narrow waterways of the CAA are occurring. As a result, the 2016 sea ice flux reached 161,000 km^2 [26].This increase indicates a trend of increased sea ice export as the amount of first year ice continues to rise.

1.4 Thesis Motivation

The continuing Arctic sea ice decline will make the Arctic Ocean regularly accessible to commercial shipping through the Northwest Passage in the summer months by the middle of the century [27]. As the Arctic Ocean continues to near the point of having ice-free summers, a substantial portion of global shipping will be looking to take advantage of the opening water to cut thousands of kilometers off of their journeys. In particular, supertankers too big to traverse the Panama Canal will want to use the Northwest Passage instead of traveling around the tip of South America [28]. The melting of sea ice also increases the susceptibility of the Arctic's natural resource deposits to human exploitation through increased accessibility. The commencement of drilling for oil and natural gas deposits would harm the natural environment and further increase the severity of the impacts of climate change which are already being felt most strongly in the Arctic [11]. As the Arctic Ocean sea ice continues to

melt due to global warming, the makeup of the ice also changes. The Arctic Ocean has lost more than 50% of multi-year ice area as of 2018 with less than 33% of the Arctic Ocean still covered by multi-year ice [29]. As the extent of multi-year ice decreases and the extent of seasonal ice increases, a number of changes will take place. Firstly, the amount of ambient noise resulting from biological life will increase due to the increased access to air at the ocean surface making it easier for air-breathing animals to live in the Arctic Ocean [13]. The amount of biomass in the Arctic Ocean is also likely to increase as a result of more direct sunlight reaching the ocean for a larger portion of the year as large plankton blooms are common in areas where the sea ice melts over the summer [30].

The changing sea ice composition has implications for defense purposes as well. Reverberation resulting from the interactions of sound waves with the bottom of the sea ice is the principal source of ambient noise in the Arctic Ocean [13]. The strength of acoustic reverberation is dependent on the type of ice the sound waves interact with. Multi-year ice produces stronger reverberation due to its rough bottom surface while first-year ice, which has a smoother bottom surface, produces weaker reverberation [31]. The severity of the reverberation increases as frequency increases which can impact the performance of acoustic homing devices such as active acoustic torpedoes [13].

The current Government of Canada defence policy *Strong, Secure, Engaged*, outlines the importance of developing increased surveillance capabilities in the Arctic to enhance situational awareness in the region [32]. The policy outlines initiatives to increase investment in space-based and surface-based assets to enhance Canada's military presence in the Arctic [32]. A space-based acoustic surveillance system for the Arctic Ocean would lend benefits to Canada that can help offset the challenges and changes a warming Arctic is expected to bring. For defense and sovereignty purposes, an Arctic acoustic surveillance system can provide Canada with enhanced abilities to monitor shipping traffic through the Northwest Passage and to detect any hostile submarines trying to enter Canada's waters under the Arctic sea ice. This information can lead to rapid deployment of resources to deal with a military threat or an illicit shipping operation. For scientific purposes, an acoustic surveillance system in the Arctic Ocean can help further research into the changing sea ice composition and its resulting effects by examining backscatter strengths and changes in regional acoustic propagation properties. It can also aid in estimating biomass content in the Arctic Ocean year-round in more areas at once.

1.5 Thesis Outline

This thesis proposes a satellite augmented acoustic surveillance system for the Canadian Arctic. The use of satellites for relaying acoustic data collected by listening devices installed at multiple points of strategic interest allows for near real-time situational awareness of the Canadian Arctic. The feasibility of such a system is investigated through an analysis of existing satellite and ground system capabilities. Multiple satellite constellation configurations are presented, and a preferred solution is selected. Additionally, a mission concept for a 3U CubeSat demonstrating the feasibility of using a lower Earth orbit (LEO) satellite to receive acoustic data from a ground-based sensor and relay that data to a ground station for analysis is presented. This mission will also give future Royal Military College of Canada (RMC) hands-on experience with satellite design, assembly, integration, and testing, as well as with on-orbit operations and acoustic data analysis.

Chapter 2 of this thesis describes the water masses and currents of the Arctic Ocean as well as its bathymetry and the effects of climate change in the area. Chapter 3 provides an overview of underwater acoustics and then focuses on considerations for the Arctic Ocean environment. Chapter 4 discusses hydrophone technology and the limitations it imposes on the proposed surveillance system. The selected locations for the hydrophones and their associated challenges are also discussed here.

In Chapter 5, different constellation configurations and the selected ground station locations are presented. Coverage gaps and expected data latency periods for the different constellations are also detailed. Chapter 6 presents a detailed satellite mission analysis and preliminary design review for the satellites based on the preferred constellation option to include orbital selection, subsystem requirements and selection, and a concept of operations. Chapter 7 summarizes the system proposal as well as its benefits and limitations.

2 Arctic Oceanography

2.1 Arctic Bathymetry

The Arctic Ocean accounts for approximately 4.3% of global ocean area but only makes up 1.4% of the global ocean volume [33]. This occurs as a result of multiple factors. Firstly, the Arctic Ocean is the smallest of the world's oceans by area and volume. Secondly, its volume is further reduced by the extensive continental shelf area that rests beneath the ocean surface at an average depth that rarely exceeds 200 m and accounts for 53% of the ocean floor [34]. There are two continental shelves surrounding the Arctic Ocean, the Canadian Arctic shelf that underlies the CAA, and the Russian continental shelf comprised of the Barents, Chukchi Sea, and Siberian shelves [33]. Figure 2.1 illustrates the extent of the continental shelf area that is present in the Arctic Ocean.
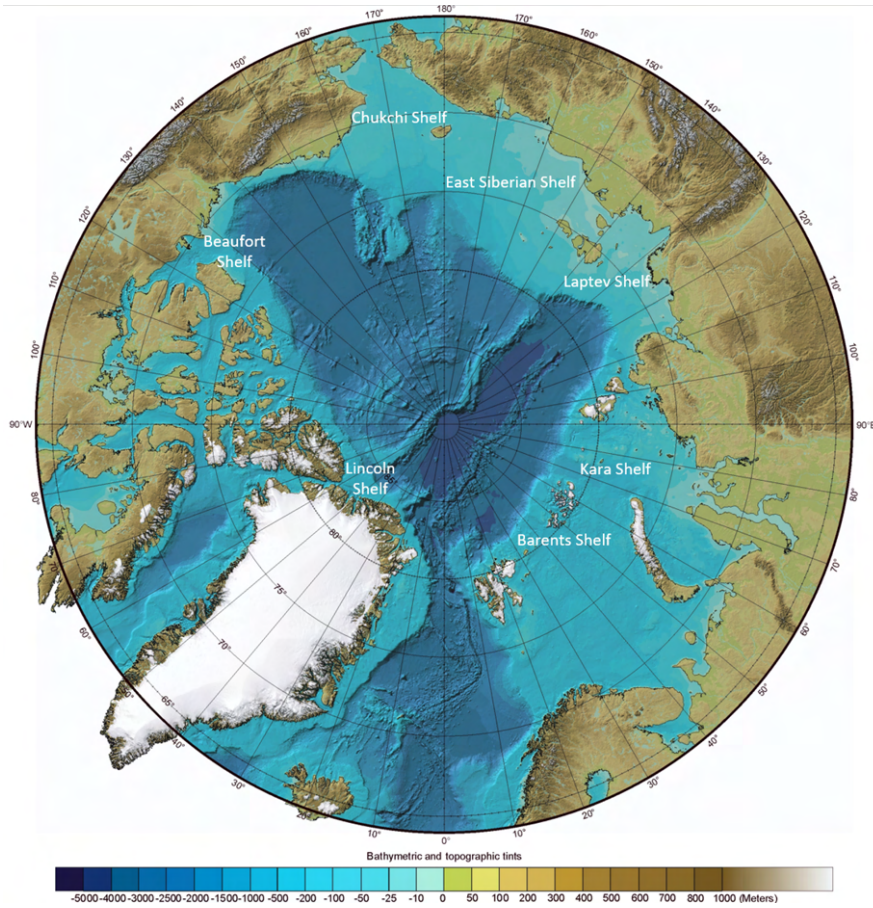
Figure 2.1: Map of the Arctic Ocean with surrounding continental shelves labelled. Adapted from the International Bathymetric Chart of the Arctic Ocean [35].

The Arctic Ocean Basin is the area that is bordered by the continental shelves surrounding the Arctic. It is variable in depth and separated into two smaller basins, the Eurasian Basin, and the Amerasian Basin, by the Lomonosov Ridge which is an underwater ridge that spans approximately 1,800 km across the central Arctic Ocean from the edge of the Siberian shelf to Ellesmere Island. It ranges from 60 to 200 km wide and rises approximately 3,700 m above the 4,200 m deep seabed [34, 36]. Figure 2.2 presents the major bathymetric features of the Arctic Ocean.
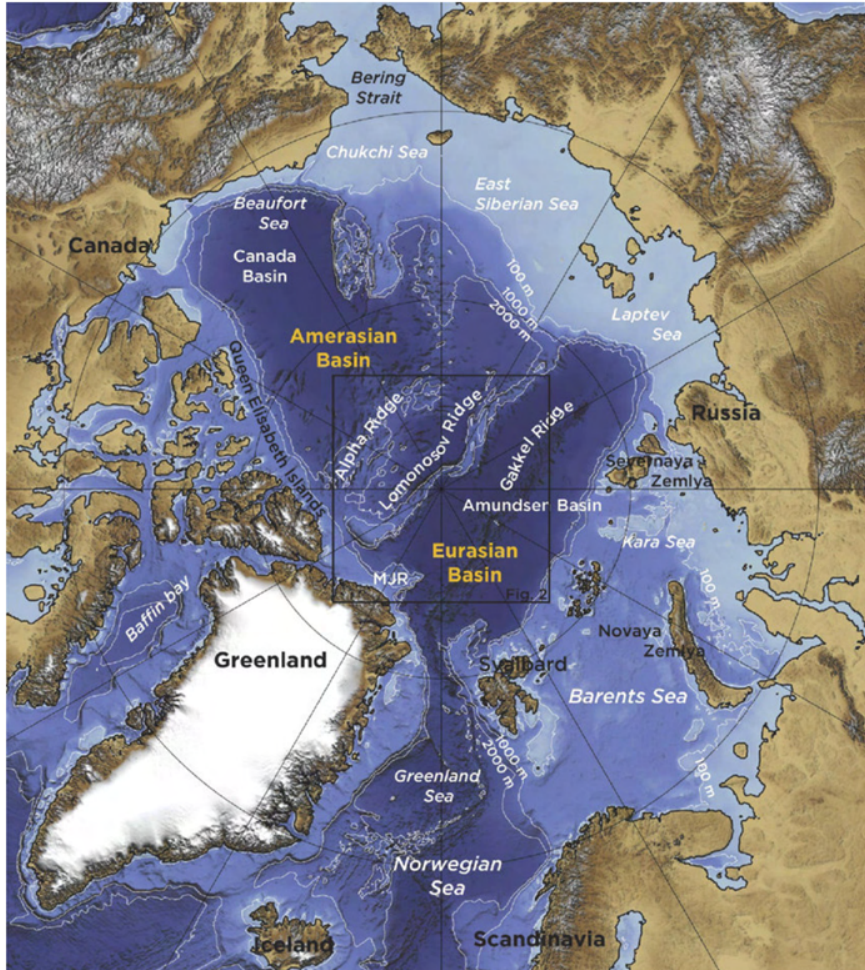
Figure 2.2: Map of the Arctic Ocean with major bathymetric features labelled [37].

The Eurasian Basin is bounded by the Lomonosov Ridge, Greenland, and the Russian continental shelf. It is split into two smaller basins, the Amundsen Basin and the Nansen Basin, by the Gakkel Ridge [33]. The Amundsen Basin is the deepest plane in the Arctic Ocean with an average depth of 4.4 km and is situated around the geographic North Pole [38]. The Amerasian Basin is located on the other side of the Lomonosov Ridge and is bounded by the CAA, Alaska, the Bering Strait, and Eastern Russia. It is further divided into the Canada and Makarov Basins by the Alpha Ridge [39].

2.2 Arctic Ocean Water Masses

Due to its relative isolation from the rest of the oceans of the world, the Arctic Ocean contains a system of water masses that is more complex than those of other oceans. The top layer of water in the Arctic Ocean, known as the Polar Mixed Layer (PML), extends to a depth of approximately 50 m and is characterized by a mixing of salty ocean water and fresh water from the numerous rivers that feed into the Arctic Ocean [40]. This layer is the coldest of all the water masses found in the Arctic Ocean as the fresh water raises its freezing point. It is also where sea ice freezes and melts seasonally, varying the salinity of the water as it does so [41]. Below the PML reside the Pacific and Atlantic Halocline layers. The halocline is a region where the temperature and the salinity of the water increase with depth. The Pacific Halocline begins at a depth of 50 m and extends to a depth of approximately 120 m [42]. The Pacific water is less dense than the Atlantic water due to its higher temperature and lower salinity and therefore resides above the Atlantic water. The Atlantic Halocline extends down to a depth of 200 m and sits below the Pacific Halocline in the western Arctic Ocean [41]. In the eastern Arctic Ocean where the Pacific Halocline fails to extend, the Atlantic Halocline resides directly below the PML. The Atlantic-Pacific Halocline boundary is found very close to the geographical North Pole [42]. The Atlantic water region is found below the Atlantic Halocline and extends to a depth of approximately 900 m. This water flows into the Arctic Ocean through the Fram Strait from the North Atlantic Current and sinks below the halocline. This is due to the increased freshwater presence around the surrounding continental shelves and the lack of freshwater near Fram Strait [43]. This is the largest inflow of water to the Arctic Ocean and creates the Arctic Boundary Current [43]. The Atlantic water mass is warmer than the surface water, exhibiting an average temperature of 3°C, but remains beneath it due to the increased salinity elevating density [43].

Below the Atlantic water sits the deepest layer of water in the Arctic Ocean, known as the Arctic bottom water, which begins at a depth of approximately 900 m and extends to the ocean floor. The Arctic bottom water has two principal sources. The first is Pacific water inflow through the Bering Strait and Chukchi Sea. The surface of this water freezes during periods of cold winter winds and the ice is pushed back out into the Bering Strait. The water that is left is denser than the PML due to its increased salinity which allows it to sink below the upper water masses as the continental shelf drops off [41].The second source is the Greenland Sea deep water which circulates into the Arctic Ocean via increased convection during cold winter temperatures

that allow the water to become denser and sink below the warmer halocline waters [40]. Figure 2.3 displays the different water masses of the Arctic Ocean.
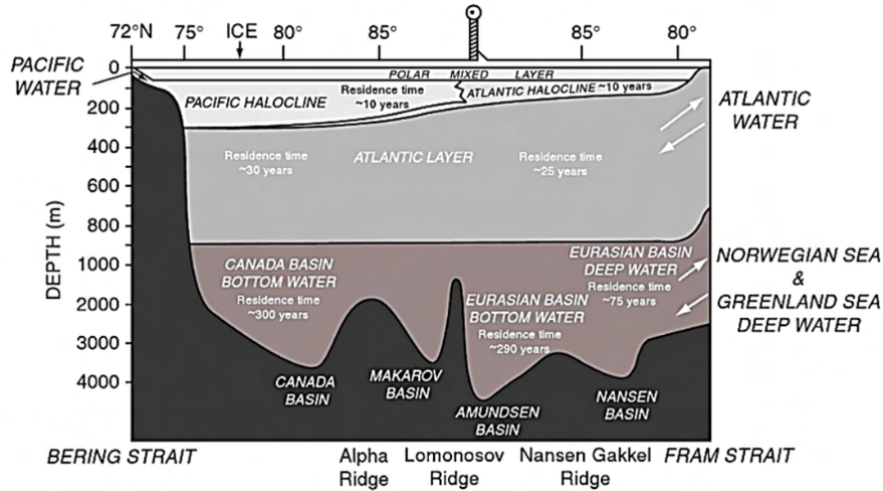
Figure 2.3: Arctic Ocean water masses and general bathymetry. Residence times refer to the length of time the water in a particular area stays there before being replaced [44].

2.3 Arctic Ocean Deep Water Circulation

Ocean water enters the Arctic Ocean through two main paths. The first is through the Bering Strait and Chukchi Sea from the Pacific Ocean and the second is through the Fram Strait from the North Atlantic Ocean. There is a negligible amount of deep-water exchange between the Atlantic and Pacific sides of the Arctic Ocean due to the Lomonosov Ridge. On the Pacific side, the Bering Strait is a shallow entry point which permits a limited amount of deep-water circulation in the Amerasian Basin. It is estimated that the deep-water in the Amerasian basin has a residence time that ranges from 200 to 600 years [45].

On the Atlantic Side, a large amount of deep water enters through the Fram Strait propelled by the North Atlantic Current. The dense deep-water sinks down to the bottom of the Eurasian Basin where it eventually reverses direction and is carried back into the North Atlantic via the East Greenland Current. The residence time of deep-water in the Eurasian Basin is estimated

13

to be between 150 and 300 years [45]. Figure 2.4 illustrates the circulation of deep water in the Arctic from the Atlantic and Pacific Oceans.
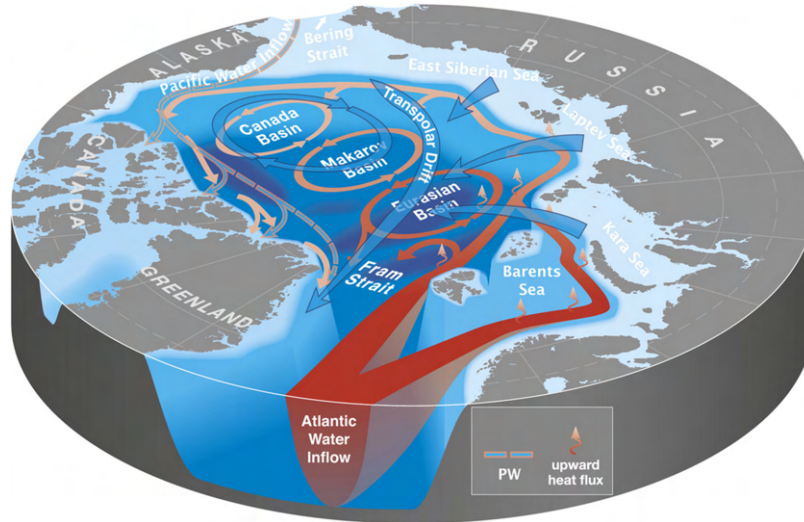
Figure 2.4: Overview of ocean currents in the Arctic. Deep Pacific water circulation is shown with the dotted blue line and Atlantic deep water circulation is shown as the dark red lines. The Beaufort Gyre is shown as the unlabelled blue circulation [46].

2.4 Arctic Ocean Surface Currents

The Arctic Ocean has two major surface currents, the Beaufort Gyre and the Transpolar Drift Current. The Beaufort Gyre is situated north of Alaska and western Canada. It is a wind-driven surface current that circulates clockwise in the Amerasian Basin and the Beaufort and Chukchi Seas. It transports thick multi-year ice from the central Arctic Ocean to the Beaufort and Chukchi Seas [47]. The Transpolar Drift Current is also wind-driven and transports large amounts of sea ice from the East Siberian and Laptev Seas through Fram Strait down the east coast of Greenland where it meets the East Greenland Current [41]. These two currents directly connect the Arctic and North Atlantic Oceans.

The Norwegian Atlantic Current is a major wind and salinity driven water inflow source of the Arctic Ocean that splits into two branches. The Barents Sea Branch enters the Barents Sea and continues past the northern coast of Scandinavia and partially enters the Kara Sea where it meets the Arctic

14

Ocean. The rest of the water flows west along the West Spitsbergen Current until it reaches the north edge of the Barents Sea where it turns east and flows into the Arctic Ocean [47]. Figure 2.4 provides a visual representation of the surface currents in the Arctic Ocean.
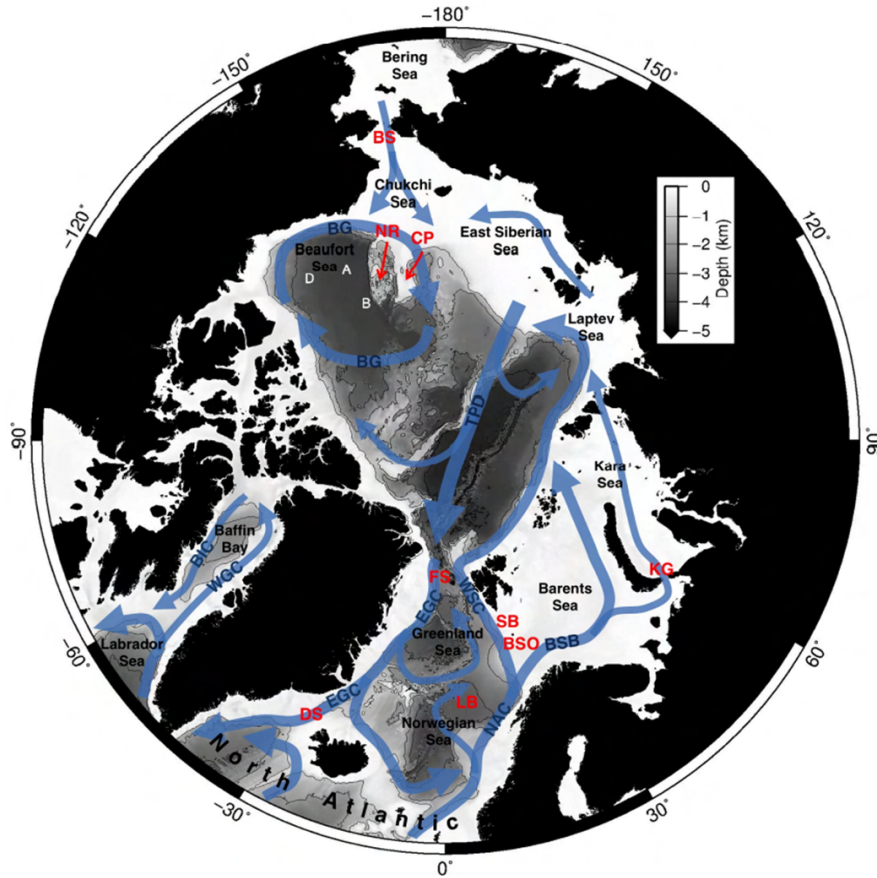
Figure 2.5: A map of the Arctic Ocean overlayed with surface currents shown as blue arrows. Abbreviations for the surface currents are as follows: WGC-West Greenland Current, BIC-Baffin Inland Current, EGC-East Greenland Current, NAC-Norwegian Atlantic Current, BSB-Barents Sea Branch, WSB-West Spitsbergen Current, TPD-Transpolar Drift Current, BG-Beaufort Gyre. Notable bathymetric features are labelled in red. Abbreviations for the bathymetric features are as follows: DS-Denmark Strait, LB-Lofoten Basin, BSO-Barents Sea Opening, SB-Svalbard Bank, KG-Kara Gate, FS-Fram Strait, CP-Chukchi Plateau, NR-Northwind Ridge, BS-Bering Strait [47].

15

3 Underwater Acoustics

3.1 Physics of Sound Propagation

The use of sound for underwater detection over radar results from the rapid absorption of radio frequencies underwater. The linear wave equation for pressure is derived from retaining the first-order terms of the conservation of mass equation, Newton's Second Law, and the adiabatic equation of state which are respectively

$$\frac{\partial \rho^{'}}{\partial t} = -\nabla \cdot (\rho_o \mathbf{v}), \tag{3.1}$$

$$\frac{\partial \mathbf{v}}{\partial t} = -\frac{1}{\rho_o}\nabla p^{'}(\rho), \tag{3.2}$$

$$\frac{\partial p^{'}}{\partial t} = c^2 \left(\frac{\partial \rho^{'}}{\partial t} + \mathbf{v} \cdot \nabla \rho_0 \right), \tag{3.3}$$

where c is the speed of sound, ρ is the density of the medium, $\mathbf{v}$ is the particle velocity, and p is the pressure [48]. By assuming the density of the medium is constant, the linear wave equation for pressure is obtained as

$$\nabla^2 p - \frac{1}{c^2}\frac{\partial^2 p}{\partial t^2} = 0 \tag{3.4}$$

[48]. It is useful to convert the wave equation to the frequency domain by through the use of the frequency-time Fourier transform pair

$$f(t) = \frac{1}{2\pi} \int_{-\infty}^{\infty} f(\omega)e^{-i\omega t}\, d\omega, \tag{3.5}$$

16

$$f(\omega) = \frac{1}{2\pi} \int_{-\infty}^{\infty} f(t)e^{i\omega t}\,dt \tag{3.6}$$

where ω is the angular frequency [48]. This leads to the frequency-dependent wave equation, also known as the Helmholtz equation

$$\left[\nabla^2 + \left(\frac{\omega}{c(\mathbf{r})}\right)^2\right]\psi(\mathbf{r},\omega) = f(\mathbf{r},\omega) \tag{3.7}$$

where ψ is the displacement potential [48]. The forces of importance to underwater acoustics are acoustic sources, both natural and artificial, which are local by nature [48]. The majority of the ocean environment is therefore sourceless which satisfies the homogeneous Helmholtz equation

$$\left[\nabla^2 + \left(\frac{\omega}{c(\mathbf{r})}\right)^2\right]\psi(\mathbf{r},\omega) = 0 \tag{3.8}$$

[48].

Sound travels much faster underwater due to the higher density of the medium. In the ocean, the speed of sound is dependent on temperature, salinity, and pressure. Since pressure is a function of depth, the speed of sound in ocean water can be approximated in terms of temperature, salinity, and depth as

$$c = 1449.2 + 4.6T - 0.055T^2 + 0.00029T^3 + (1.34 - 0.01T)(S - 35) + 0.016z \tag{3.9}$$

where c is the speed of sound in meters per second (m/s), T is temperature in degrees Celsius (°C), S is salinity in practical salinity units (PSU), and z is depth in meters (m) [49]. In general, as the frequency of sound waves increases, the transmissibility of those waves decreases due to the accelerated rate of energy loss during travel and as a result of interference with the surface or the ocean bottom [50].

In the non-polar regions of the ocean, the sound speed is higher near the surface due to increases in sea surface temperature throughout the day from solar insolation. In the open ocean, near-surface mixing due to wind and wave activity is a common occurrence. This leads to a mixed layer of water that is isothermal [51]. In this isothermal layer, sound speed increases with depth due to the increased pressure found further beneath the surface until the sonic layer depth is reached. The sonic layer depth is the depth near the surface at which a local maximum of the sound speed profile occurs. Below the isothermal layer

lies the thermocline where the temperature decreases with depth. This causes the sound speed to decrease in this region. Finally, below the thermocline, there is a large region of constant temperature where the sound speed slowly increases with depth due to the increased pressure [51]. As a result of the presence of the thermocline between the deep isothermal layer and the near-surface mixed layer, the creation of the Deep Sound Channel occurs. The Deep Sound Channel is found at the axis of minimum sound speed on the sound speed profile and acts as a waveguide [52]. A seasonal thermocline is an extension of the main thermocline which varies in depth with the seasonal changes in solar radiation that occur throughout the year [52]. Figure 3.1 displays a typical ocean sound speed profile.
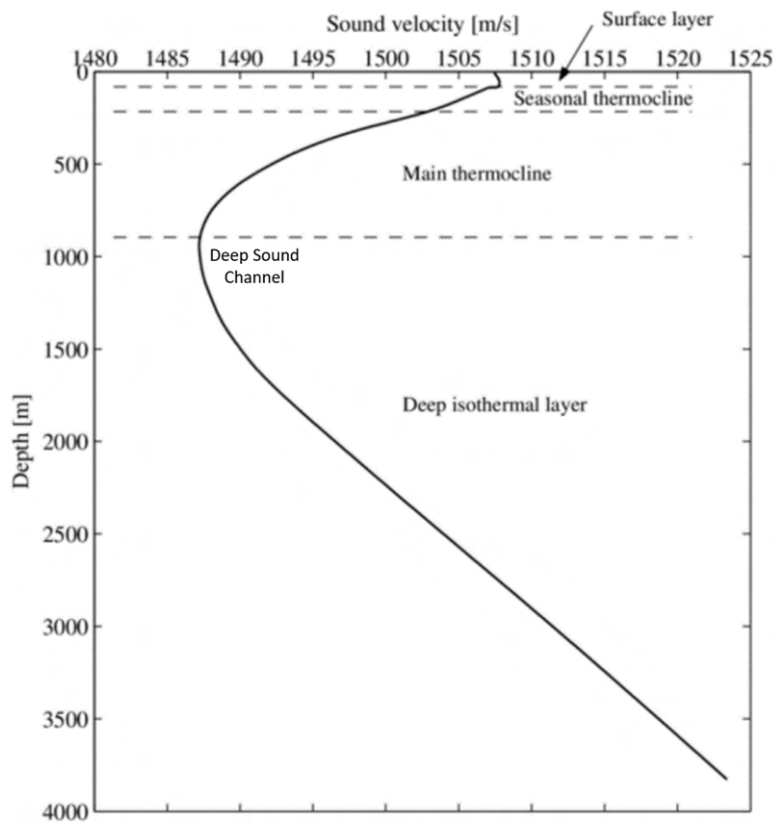
Figure 3.1: A typical ocean sound speed profile with labels included for the associated components. The seasonal thermocline is a small layer directly above the main thermocline that changes in depth throughout the year as solar insolation varies seasonally. Adapted from A. T. Johannson [51].

By using the information given by ocean sound speed profiles, the path of a sound ray can be predicted using a modified version of Snell's Law which considers the ocean water to be a medium consisting of many thin layers of water with varying sound speeds [52]. Equation 3.4 states Snell's Law of refraction for underwater sound waves as,

$$\frac{cos(B_1)}{cos(B_2)} = \frac{C_1}{C_2} \tag{3.10}$$

where B_1 is the angle between the horizontal boundary and the incident sound ray, B_2 is the angle between the horizontal boundary and the refracted sound ray, and C_1 and C_2 are regions of different sound speeds. From this relationship, it can be deduced that sound waves will bend toward the layer with the lower density as sound waves tend to refract toward less dense mediums [52]. Propagation for frequencies less than 10 Hz is dependent on the composition of the ocean floor as frequencies in this range are increasingly susceptible to interactions with the bottom of the ocean [53]. As frequencies approach 1 MHz losses in signal strength increase to hundreds of dB per km making frequencies in this range difficult to use over long ranges [54].

3.2 Ray Paths

Depending on the location of the underwater source in relation to the local sound speed profile, emitted sound rays can take different paths away from the source. The most straightforward case is a direct ray path from the source to the target. In this case, the ray travels directly to the target while avoiding any interactions with the ocean floor or reflections from the surface [52]. If the source is below the sonic layer depth, the angle at which sound rays must be emitted to reach a target at or near the surface must be high in order to prevent the downward bending of sound rays by the increasing sound speed. If the source is above the sonic layer depth, the range of angles from which sound waves can be emitted is much wider as the vast majority of the waves will be refracted upwards due to the sound speed decreasing towards the surface [55]. This path is useful for shorter range communication and detection as sound waves that follow a direct path do not commonly travel more than tens of km depending on frequency [55].

In the isothermal near-surface mixed layer of ocean water, sound speed briefly increases with depth [51]. When a sound ray travels from a source through this mixed layer, it is refracted towards the surface where it reflects and is forced downward where it once again is refracted back upwards by the

increasing sound speed. This phenomenon is known as surface ducting and can result in sound waves travelling distances on the order of hundreds of kilometers [56]. This creates a gap in coverage known as the shadow zone and is shown in Figure 3.2 [57]. This gap is commonly exploited by submarines looking to avoid detection and is a key consideration in the design of acoustic surveillance systems [57].
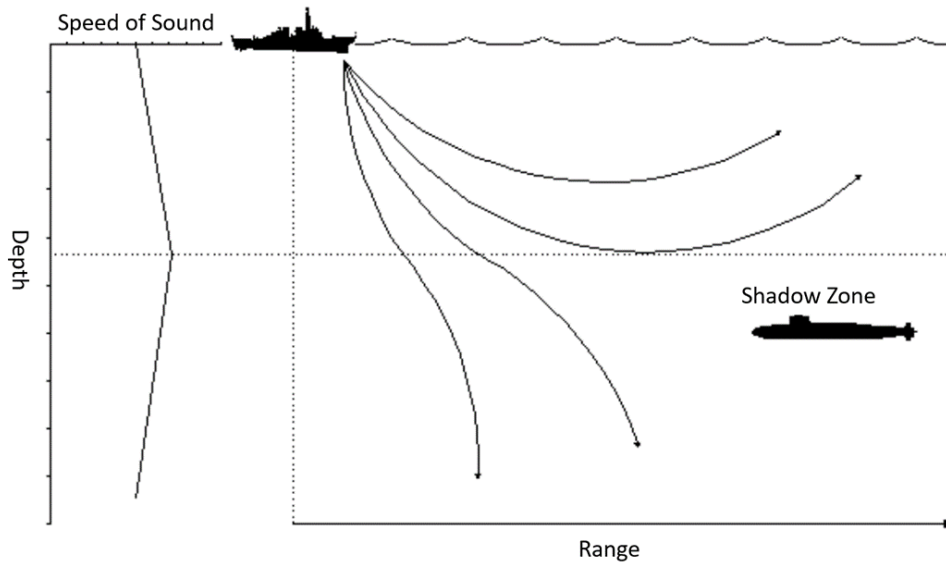
Figure 3.2: An illustration of the formation of a shadow zone between a surface duct and downward refracted sound waves. The axis of maximum sound speed is indicated by the dotted line. Adapted from the Military Analysis Network [58].

Bottom bounce occurs when a ray hits the bottom of the ocean and is reflected back towards the surface. It is then possible for the ray to reflect back down to the bottom and repeat the cycle. This cycle cannot be sustained as long as surface ducting due to transmission loss incurred by striking the bottom of the ocean [59]. This propagation method is therefore not able to travel as far as surface ducting but can still travel distances on the order of tens of kilometers depending on the local bathymetry [59].

A convergence zone occurs when sound rays emitted together are refracted along similar paths and reach the surface at a specific location [60]. They result in areas of high sound levels due to the focusing of sound waves. The receiver,

however, must be located within the convergence zone to detect noise as the waves are reflected back downwards upon reaching the ocean surface [60]. The refraction of sound waves toward the bottom of the ocean followed by an upward bend toward the surface as a result of the increasing sound speed in the deep ocean is a common path due to the similarity in sound speed profiles in temperate oceans [60]. Multiple convergence zones are possible as sound waves reflect off of the ocean surface and begin a cyclical pattern in which they are refracted back to the surface after taking a similar path to the one taken from the source. The number of convergence zones is limited, however, due to energy loss and scattering from striking the surface [60]. Another limitation of convergence zone propagation is that for long range targets, the sound waves must travel down a significant distance in order to be refracted up to a distant target. This increases the risk of interference from the ocean bottom which can alter the path of the sound waves and result in further energy loss and scattering [60]. Figure 3.3 illustrates the creation of a convergence zone.
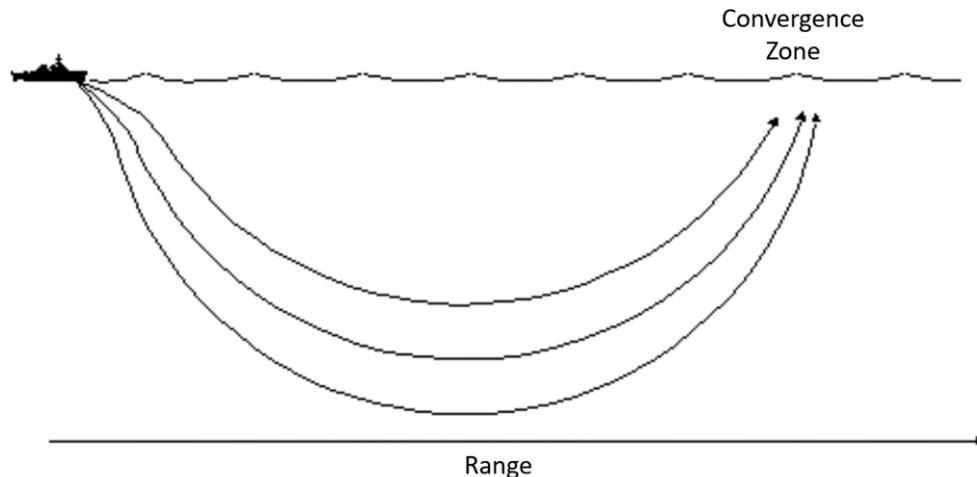
Figure 3.3: An illustration of the formation of a convergence zone between. Adapted from the Military Analysis Network [58].

The deep sound channel, also known as the sound fixing and ranging channel (SOFAR), occurs at the layer of water where the sound speed profile is at a minimum. This region of the ocean acts as a waveguide within which waves oscillate between top and bottom boundaries which are defined either by local sound speed maximums or the continuous increase in sound speed found

in the deep ocean [61]. Waves emitted in this channel can travel extremely long distances as they do not encounter interference and loss of energy from the bottom of the ocean or the surface. An experiment conducted with deep sound channel hydrophones in the Pacific Ocean found that multiple explosions detonated within the deep sound channel were detected approximately 16,000 km away [61].

3.3 Arctic Ocean Acoustic Propagation

The acoustics of the Arctic Ocean differ from temperate oceans in a number of ways. Due to the reduced amount of solar radiation absorbed by the Arctic Ocean and the presence of sea ice, the isothermal layer that is found near the surface of other oceans, such as the Atlantic and Pacific, is either greatly diminished or entirely eliminated [62]. The Arctic Ocean also exhibits two differing sound speed profiles on either side of the Lomonosov Ridge [63].

Generally, the speed of sound continuously increases with depth in the eastern Arctic Ocean, though a temperature maximum can at times be found between 300 m and 900 m due to the Atlantic water entering through Fram Strait [62]. This happens as a result of the Atlantic water being warmer than the Arctic surface water since the water at the surface of the Arctic Ocean is mixed with fresh water from numerous inflow points, giving it a higher freezing point that results in the formation of sea ice [41]. The result of a monotonically increasing sound speed profile is the occurrence of upward sound wave refraction from any depth in the ocean. This causes sound waves emitted in this region to repeatedly interact with the often-ice-covered ocean surface [63]. These interactions reflect the waves back downward where they are eventually refracted back toward the surface, which is known as half channel propagation and is illustrated in Figure 3.4 [64]. Though the sound waves are reflected when they interact with the ice, they also lose energy and can be scattered by the rough, uneven surface at the bottom of the sea ice [63]. The losses incurred through interactions with the sea ice increase as frequency increases, with frequencies up to approximately 30 Hz able travel distances of hundreds of km [65].
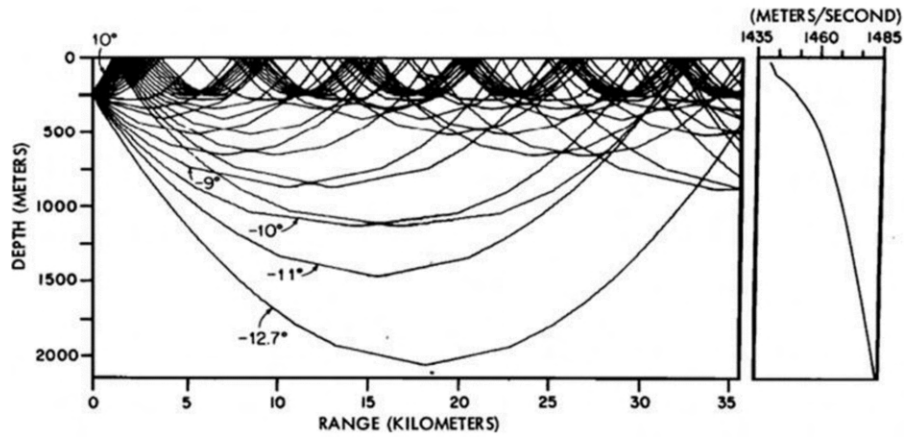
Figure 3.4: A ray path diagram showing half channel propagation in the eastern Arctic Ocean at different emission angles with a corresponding sound speed profile displaying a monotonically increasing trend [64].

The propagation of sound waves in the western Arctic Ocean differs from the eastern Arctic Ocean due to the presence of an acoustic duct caused by a thermocline from the entrance of colder Pacific winter water from the Bering Strait [63]. This causes sound waves emitted within this duct to be able to travel distances up to 400 km [66]. The duct and associated sound speed profile are shown in Figure 3.5.
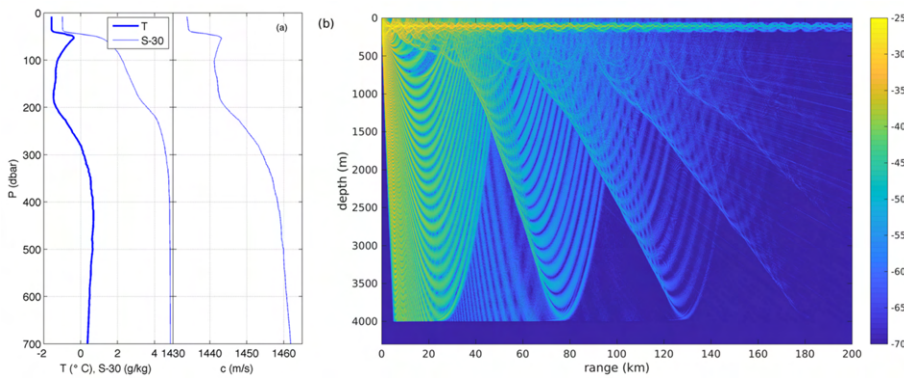
Figure 3.5: a) Temperature and salinity profiles from the Beaufort Sea. b) Transmission loss plot for a 900Hz source placed within the Beaufort Sea Pacific Water Duct between the depths of 100 m and 200 m. The colour scale indicates the magnitude of transmission loss in dB [67].

The lower frequency limit for ideal sound propagation in the Arctic Ocean is similar to that of temperate oceans at around 10 Hz as a result of signal absorption by the ocean floor [51]. The upper limit of around 50 Hz, however, is much lower than in temperate regions due to the increased interference created by the presence of the rough underside of sea ice [13]. Frequencies above 50 Hz can still propagate significant distances, although they are subject to increased scattering and energy loss by the rough sea ice. The small range of 10 Hz to 50 Hz, however, is a very useful frequency range as it overlaps with the range of 5 Hz to 30 Hz emitted by submarine propellers [13]. Figure 3.6 displays the typical acoustic profile for a submarine. Most heavy shipping vessels are found to emit noise between 20 and 80 Hz [28]. This creates a narrow but useful frequency range for a potential passive acoustic surveillance system to listen to in order to detect shipping and sub surface traffic.
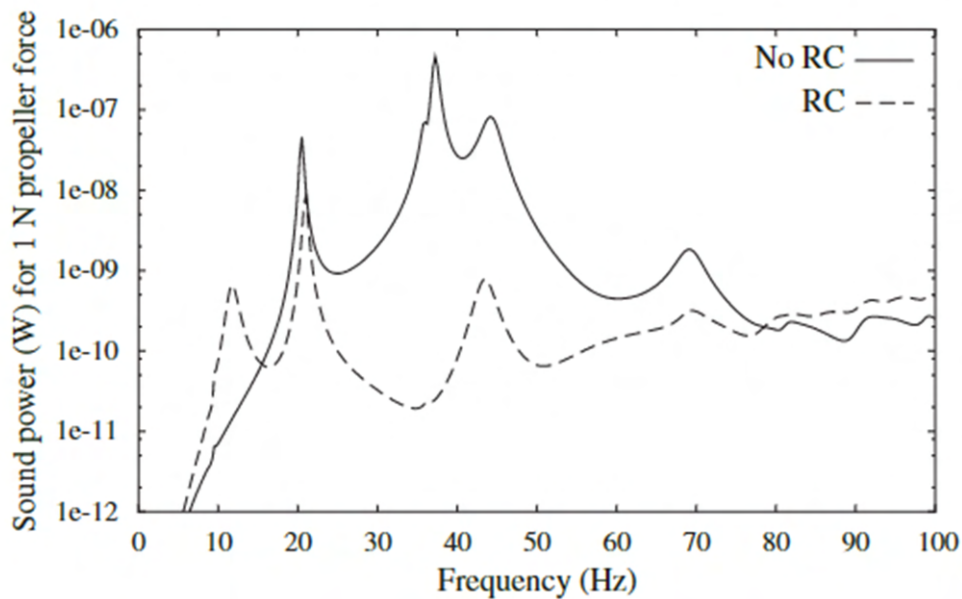
Figure 3.6: The radiated sound power of a submarine propellor and hull as a function of frequency is shown with and without a hydraulic vibration absorber known as a resonance changer (RC) [68].

3.4   Arctic Acoustic Modelling

Generally, acoustic models solve the wave equation or Helmholtz equation using a variety of techniques and approximations in order to create a spacial sound pressure or sound intensity field. Acoustic modelling in the Arctic Ocean is made difficult by the presence of sea ice. This project considers four propagation models for the modelling of propagation losses in the Arctic Ocean. PROLOS uses an adiabatic normal modes technique and works best in primarily low frequency and shallow environments since computational and memory requirements increase with the number of modes [69]. The normal modes method is capable of accurately predicting wave propagation and dispersion at ice-free interfaces but cannot conduct modelling of an ice-covered interface [69]. OASES uses a wavenumber integration technique that is capable of providing exact solutions for the acoustic environment and is capable of accurately modelling complex sediments and interfaces, as well as elastic surfaces which is beneficial for modelling the Arctic environment [48]. The range-dependent version of the model is considered to be the standard for predicting propagation loss [70]. Range-dependent refers to the ability of a model to vary the acoustic properties of the medium away from the source. A range-independent model is only able to simulate the same environmental acoustic properties at all distances from the source. Bellhop uses a Gaussian beam tracing approach that models transmission loss by tracing beam paths using high-frequency approximations [71]. Bellhop is capable of range-dependent modelling, and allows for additional input files to specify the acoustic properties of boundaries [70]. PECan uses the parabolic equation method which solves the Helmholtz equation using two approximations. First, outgoing acoustic energy is far stronger than backscattered acoustic energy which allows the backscattered energy to be ignored, and second, that at long ranges, the acoustic waves propagated at near-horizontal angles [48]. PECan is able to model very basic interactions with sea ice through the definition of a quasi-elastic layer and can be used to model deterministically rough surfaces [48].

In a shallow environment with smooth ice cover, OASES, Bellhop, and PECan were all accurate at 50 Hz and 500 Hz with Bellhop taking much longer to run [72]. Figure 3.7 displays the performance of Bellhop and PECan in comparison to OASES at 50 Hz and 500 Hz under a smooth ice surface.
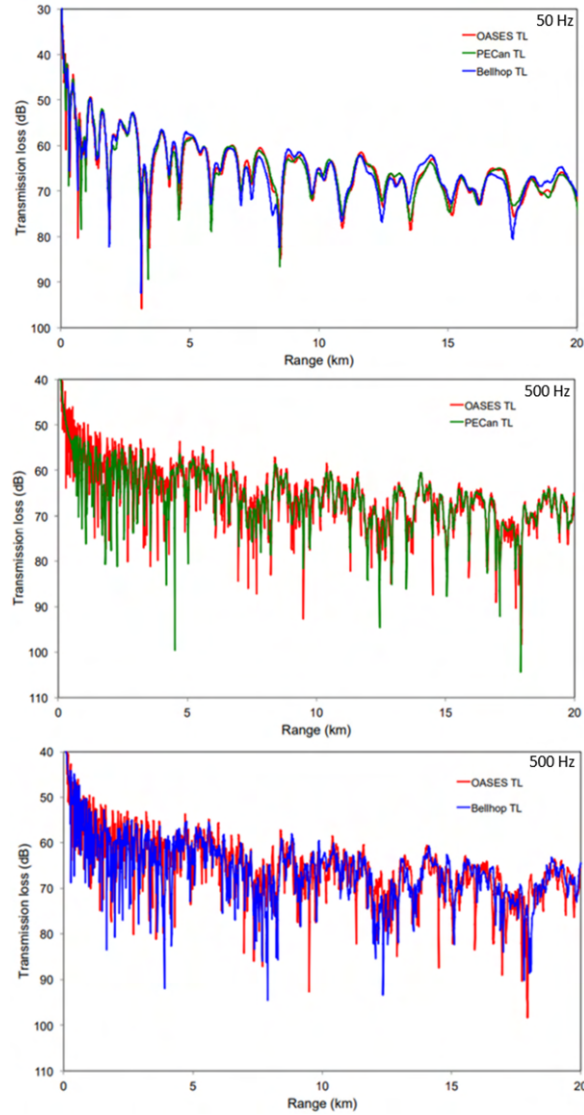
Figure 3.7: Transmission loss comparison of OASES, Bellhop, and PECan at 50 Hz under a smooth ice surface (top). OASES and PECan transmission losses at 500 Hz under smooth ice (middle). OASES and Bellhop transmission losses at 500 Hz under smooth ice (bottom). Adapted from S. Pecknold and C. Binder 2020 [72].

For a rough ice surface, Bellhop and PECan overestimated propagation losses, especially at longer distances with PECan not giving accurate results

for 50 Hz under rough ice [72]. In the deep-water scenario, Bellhop and PECan once again produced significant overestimates of propagation loss with PECan not able to converge on the rough ice and deep water scenario [72]. It can therefore be concluded that OASES is the ideal choice for range-dependent modelling of low to mid frequency propagation in ice-covered environments provided long running times are not a consideration. PECan is able to run much faster but is not accurate for rough ice scenarios. Bellhop is a middle ground that is able to converge for range-dependent smooth and rough ice scenarios but can overestimate propagation losses, particularly at longer ranges.

3.5 Arctic Ocean Ambient Noise

Sources of ambient noise in the Arctic Ocean differ from those in mid-latitude ocean regions [63]. The noise caused by the interaction between surface waves and winds is eliminated due to the presence of sea ice [13]. Most biological noise signals detected in the Arctic come from bowhead whales, beluga whales, bearded seals, walruses, and grey whales which emit sounds in the 0.05 to 20 kHz range [73]. The general extent of ambient noise levels in the Arctic is shown in Figure 3.8.
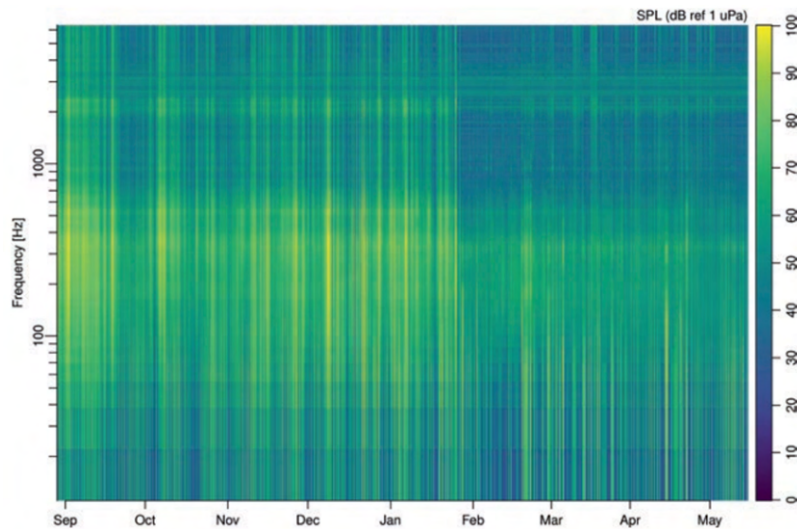
Figure 3.8: Arctic ambient noise levels recorded from September 2018 to May 2019 at the Barrow Strait Real Time Observatory. The colour scale indicates noise level in dB [73].

Noise caused by shipping activity in the Arctic Ocean is significantly lower than in other oceans due to the reduced amount of shipping activity that takes place. The amount of shipping-related noise, however, is increasing as the extent of Arctic sea ice decreases with shipping activity tripling in select southern areas of the Northwest Passage such as Hudson Bay from 1990 to 2015 [28]. The acoustic signatures of various ship types are displayed in Figure 3.9.
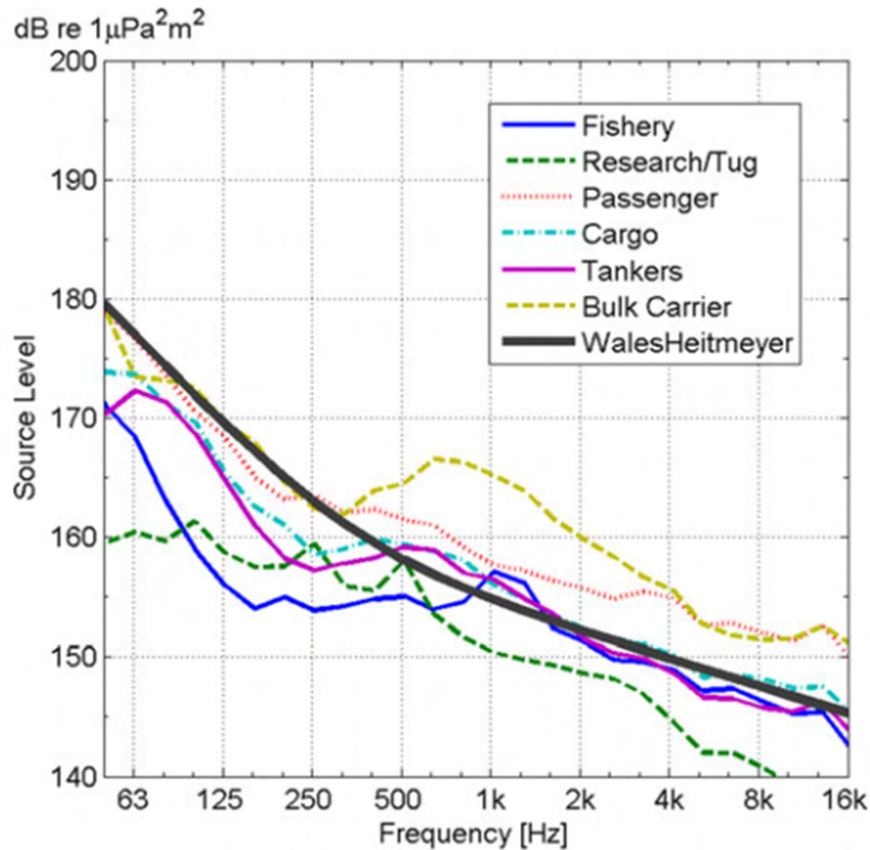
Figure 3.9: Noise level as a function of frequency for various ship types compared to the Wales-Heitmeyer model [74].

A significant source of noise in the Arctic Ocean is generated by seismic surveys which increase ambient noise by 2 to 8 dB in the western Arctic Ocean around the Beaufort Sea [13]. Another principal source of noise generation in the Arctic Ocean is the movement and cracking of sea ice generated by

surface winds, currents, and tides. Ridging, a phenomenon where large chunks of multi-year ice are piled up on top of each other, can be a significant local source of noise [13]. The levels of ambient noise in the Arctic Ocean are also highly variable depending on the local conditions with noise under sea ice ranging from 20 dB lower to 30 dB higher than the same location under ice-free conditions [66].

4 Hydrophone Systems

4.1 Hydrophone Technology Description

The hydrophone was developed to counter the threat posed by the German U-boat fleet during the Second World War. The preferred method of hydrophone deployment is from an aircraft as this allows for the greatest amount of system flexibility and mobility. In general, this passive hydrophone is designed to be dropped from an aircraft and then separate into a surface radio transmitter and an underwater acoustic sensor [75]. From there, the aircraft is able to receive and process acoustic data and potentially locate any submarines in the area. The typical frequency range for hydrophone data transmission lies in the VHF band from 130 to 173.5 MHz but can extend up into the L-band at 1.8 GHz to accommodate larger telemetry requirements [76].

The first widely used detection method employed by hydrophones was low frequency analysis and recording (LOFAR) allows an operator to make a detection of a submarine but is unable to determine its bearing or range from a single device [75]. More positional accuracy is possible with LOFAR if multiple buoys are deployed in the same area with sufficient spacing. The differing noise levels from a submarine at the different hydrophones can provide a rough estimate of the region where the submarine is located [77]. Additionally, the bearing of a target can be determined with LOFAR if two hydrophones are placed a known distance apart and a time delay between them is introduced [75]. The detection method currently used by advanced navies is directional frequency analysis and recording (DIFAR) which uses two or more directional sensors to determine the bearing of a submarine [77]. Using at least three simultaneous contact bearings, the exact position of a submarine can be triangulated [78].

Presently, the use of geobuoys in the Arctic for underwater acoustic surveillance is being explored by the Canadian Armed Forces. The geobuoys are capable of listening for sounds underwater without having to penetrate the thick, multi-year ice that is particularly prevalent in the Canada Basin and

the Beaufort Sea [79]. The geobuoys are dropped from an aircraft and are equipped with a parachute, as well as an icepick on their bottoms that sticks into the ice [79]. Once in place, the vibration sensors on the geobuoys detect underwater sounds, ambient noise, and noise from ice motion that travel through the ice and the on-board radio transmitter sends the data up to a circling aircraft [79].

4.2 Proposed Hydrophone Locations

Five areas of strategic and acoustic importance have been chosen in accordance with recommendations from Defence Research and Development Canada (DRDC) and are shown in Figure 4.1.

SITE	DEPTH (m)	LAT	LONG
A	3000	82.5 N	112.0 W
B	3500	77.0 N	135.0 W
C	1100	73.5 N	72.0 W
D	220	74.3 N	92.15 W
E	800	66.5 N	59.0 W
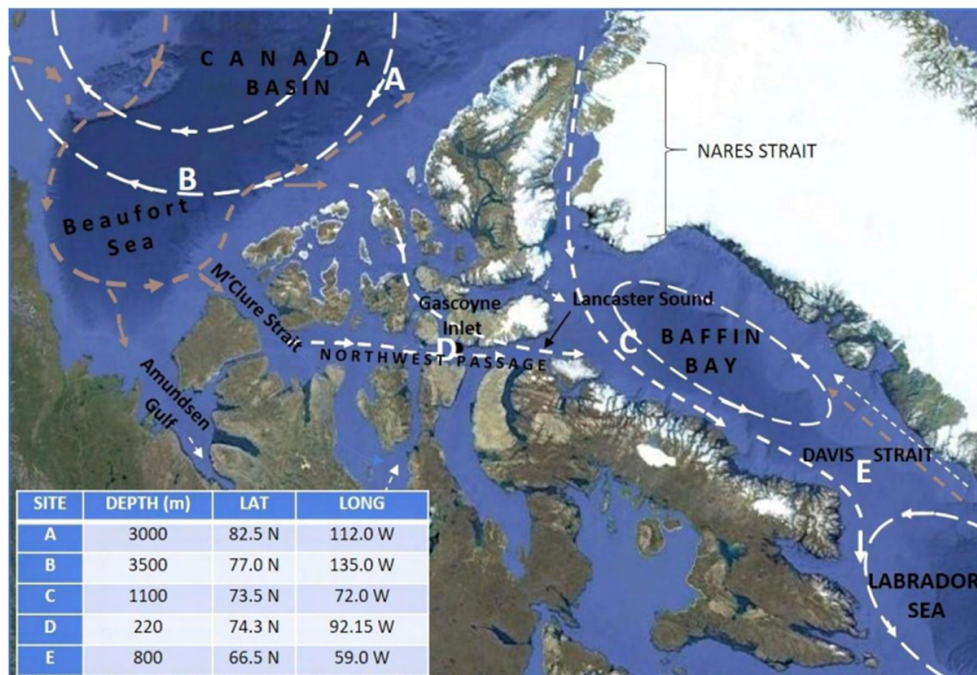
Figure 4.1: Map of strategic acoustic surveillance areas in the Canadian Arctic with associated depths and coordinates displayed. The white dotted lines indicate surface currents, and the brown dotted lines indicate deeper, warmer currents [80].

Strategic areas A and B are situated in the Canada Basin and Beaufort Sea

on the west coast of the CAA. They are characterized by year-round multi-year ice coverage with ice thickness spanning from 0.5 to 1.5 m [29]. The proportion of first-year ice in this area is increasing as multi-year ice export and melting continues to rise. From 1997 to 2021, the percentage of annual multi-year ice export through Fram Strait that originated in the Beaufort Sea increased from 7% to 33% [81]. Detection ranges in this region span from 7 to 50 km depending on the season and ambient noise levels [80]. The sound speed profiles for areas A and B are shown in Figure 4.2.
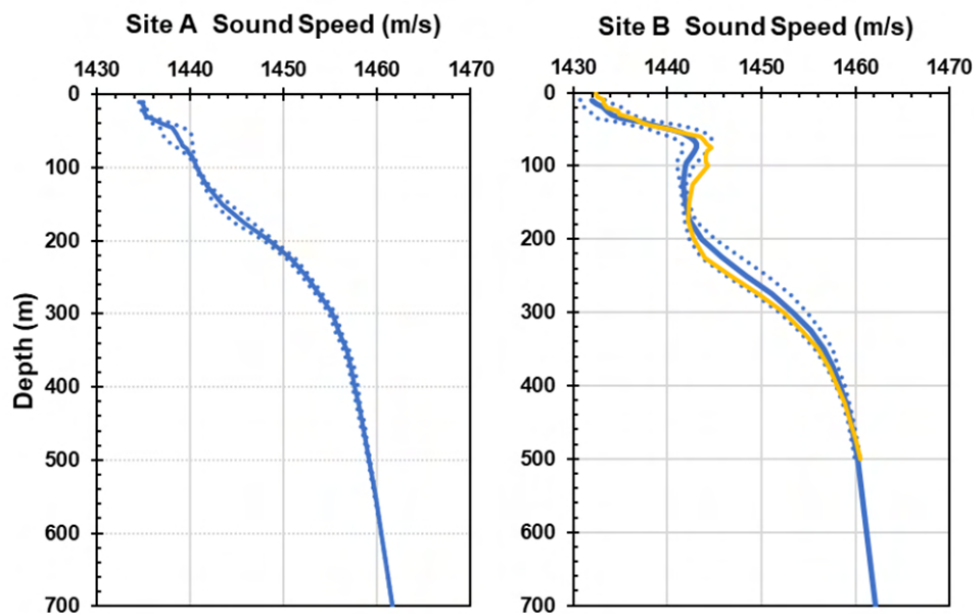
Figure 4.2: Average year-round sound speed profiles for strategic areas A and B. The dotted lines indicate one standard deviation from the mean and the yellow line for site B is an average of data collected from 2017 to 2019 [80].

The eastern Northwest Passage, for the purposes of this examination, will be considered to extend between strategic sites C and D from Gascoyne Inlet through Lancaster Sound and into northern Baffin Bay. This region is covered by sea ice between 9 and 10 months per year and is characterized by strong currents that contribute to a mobile ice field that forms an ice arch which immobilizes the ice in the region [80]. The location of this ice arch varies highly from year to year with eastern and western extremes occurring 512

km apart [82]. As with sites A and B, it is projected that the proportion of smooth, first-year ice will continue to increase in the eastern Northwest Passage as atmospheric temperatures continue to rise [83]. Detection ranges in this region vary from 55 to 110 km depending on the season and ambient noise levels [80]. The sound speed profile for the eastern Northwest Passage is shown in Figure 4.3.
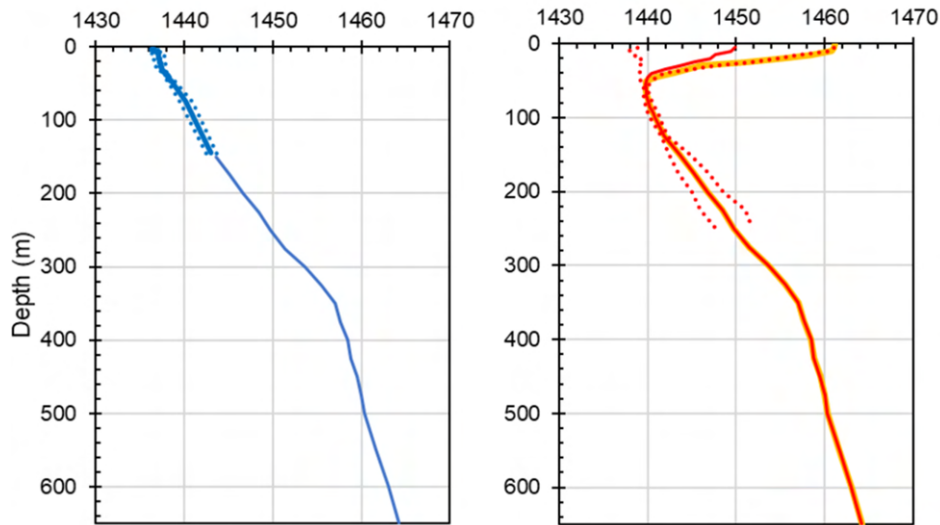
Figure 4.3: Sound speed profiles for the eastern Northwest Passage in the winter on the left and the summer on the right. The dotted lines indicate one standard deviation from the mean and the yellow line in the Summer graph shows the projected change in sound speed near the surface due to surface heating as a result of longer ice-free periods in 2040 [80].

In northern Baffin Bay, around area C, ice conditions vary from full ice coverage for most of the year to entirely ice-free from June to October [80]. The ice drifts southeast towards Davis Strait with land fast ice building up along the coasts [84]. Year-round sea ice conditions are similar in area E located in Davis Strait with ice-free conditions persisting between two and three months in the summer and ice drifts moving southwest into the Labrador Sea [85]. Moving west to east, there exists a decreasing trend in sea ice thickness and an increasing length of the ice-free season due to warm water from the Atlantic Ocean being transported northward along the west coast of Greenland by the West Greenland Current [80]. In the future, a longer ice-free season is expected resulting in a reduction in the thickness of the winter ice sheet [86]. The sound

speed profiles for Baffin Bay and Davis Strait are shown in Figure 4.4.
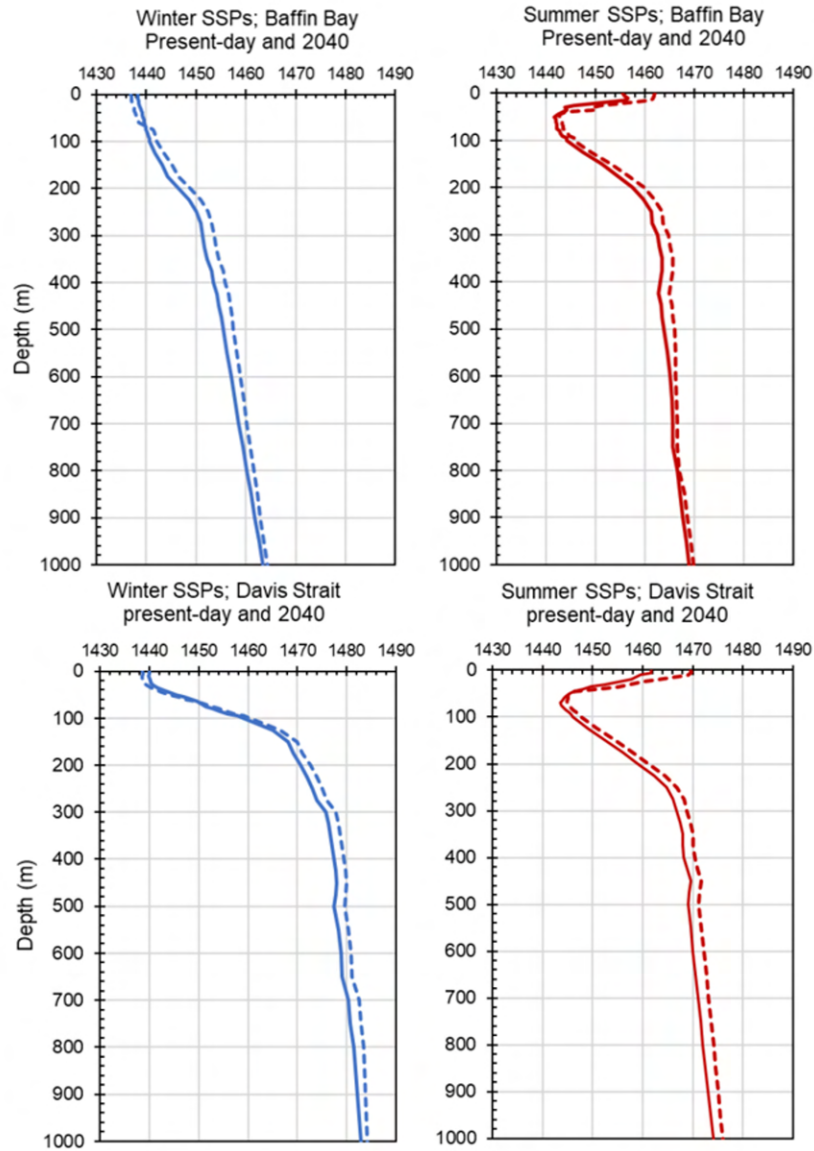
Figure 4.4: Winter and summer sound speed profiles for Baffin Bay (top) and Davis Strait (bottom). The solid lines indicate present day sound speed profiles while the dotted lines show the projected sound speed profiles for 2040 [80].

4.3 Hydrophone Deployment Considerations by Strategic Area

4.3.1 Strategic Areas A and B

In the Canada Basin and Beaufort Sea, where the year-round multi-year ice provides a stable base from where to deploy a listening device, it is important to establish where the equipment will transit during its deployment. For beacons deployed far from the CAA coastline, one year drift distances are about 500 km with deployments near the CAA coastline drifting approximately 250 km over a one year period [87]. This points to an ice-tethered vertical line array (VLA) as a good solution for local acoustic monitoring. To take advantage of the acoustic duct located between the depths 100 m and 200 m, the array must be long enough to deploy hydrophones within this region [80]. In order to find the thickest, most stable ice from which to deploy and tether the VLA, it is necessary to go beyond the edge of the ice pack where a ship can go. This would require the use of a ship-deployable helicopter to ferry personnel and equipment to the desired location [87]. The batteries required to power the VLA can be planted beneath the surface of the ice to help insulate them from extreme temperatures [87]. Figure 4.5 shows a concept diagram of an ice-tethered VLA in the Canada Basin. Provided advances in geobuoy technology allow for transmissions up to LEO satellites and detection capabilities similar to existing hydrophones, they can present a viable alternative due to a simpler deployment process that involves the buoys being dropped directly from an aircraft onto the ice [79].
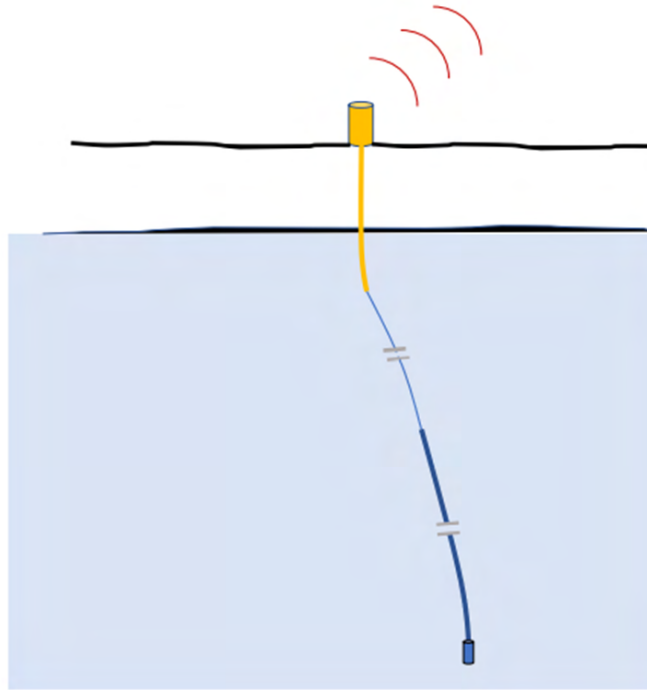
Figure 4.5: A concept diagram of an ice-tethered VLA in the year-round Canada Basin [87].

4.3.2 Strategic Areas C and E

In the northern Baffin Bay and Davis Strait region, the main challenge encountered is that of highly variable sea ice conditions throughout the year. With ice-free conditions occurring from June to October and quickly freezing over by the end of November, equipment deployed in this area must be able to be frozen in for long periods of time [87]. The strong southward currents in the Baffin Bay and Davis Strait region would reduce the transit time from area C to area E to approximately 75 days assuming the buoy is never frozen into the ice during this period [86]. If the buoy were deployed late into the ice-free season and were frozen into the mobile ice, the journey from area C to area E would increase to 150 days [87]. Since there is a substantial ice-free period in northern Baffin Bay in the summer months, it is easily accessible by ship. This makes ship-based deployments and recoveries possible which allows for larger power generation systems for the buoy which enables longer deployment times [87]. Figure 4.6 shows a concept of a free-floating buoy capable of

being frozen into the ice in Baffin Bay and Davis Strait.
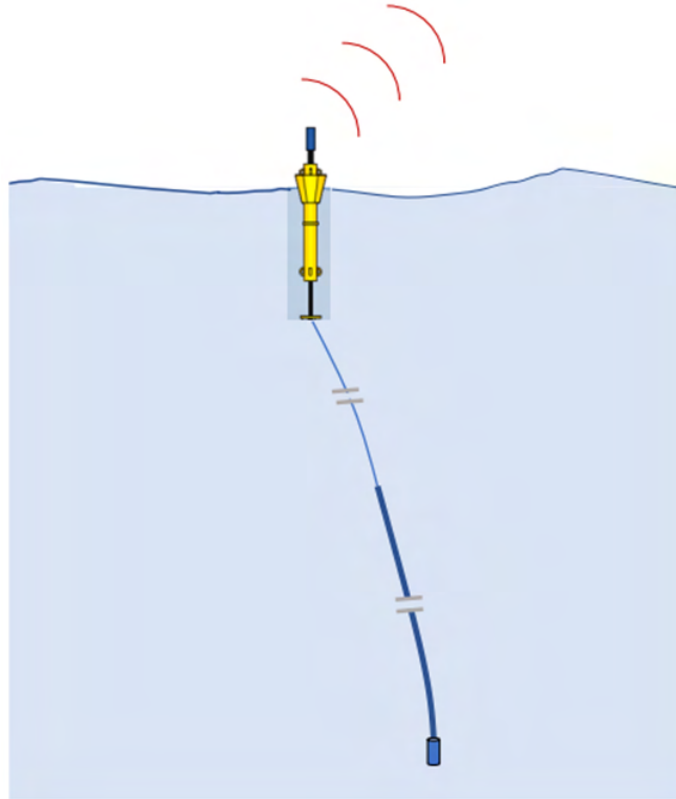
Figure 4.6: A concept diagram of a free-floating buoy capable of being ice-tethered in Baffin Bay and Davis Strait [87].

4.3.3 Strategic Area D

Similar to Baffin Bay and Davis Strait, the Northwest Passage sees two to three months of ice-free conditions from sites D to C and, depending on the year, sees the formation of an immobile ice pack [87]. An ice-tethered buoy is not viable as there is no way to predict the presence or duration of an immobile ice pack. Strong tides and eastward currents can create mobile ice flows that are capable of destroying equipment and the low depth of the Northwest Passage, especially nearer to shore, poses great risk to a mobile drifting array hitting the bottom [87]. Strong currents and surface winds contribute reduce the transit time of drifters from area D to area C to 90 days [87].

As neither a surface drifter nor an ice-tethered buoy is a viable option for this region, sub-surface moorings connected by underwater cable to a land-based relay station present the best solution [87]. There are two distinct system concepts for this solution. The first is a moored VLA that acoustically transmits data to an underwater data hub connected by cable to a land-based communications centre for satellite relay [87]. The second uses horizontal line arrays (HLA) directly connected to the land-based relay centre via underwater cable [87]. Both concepts are illustrated in Figure 4.7.
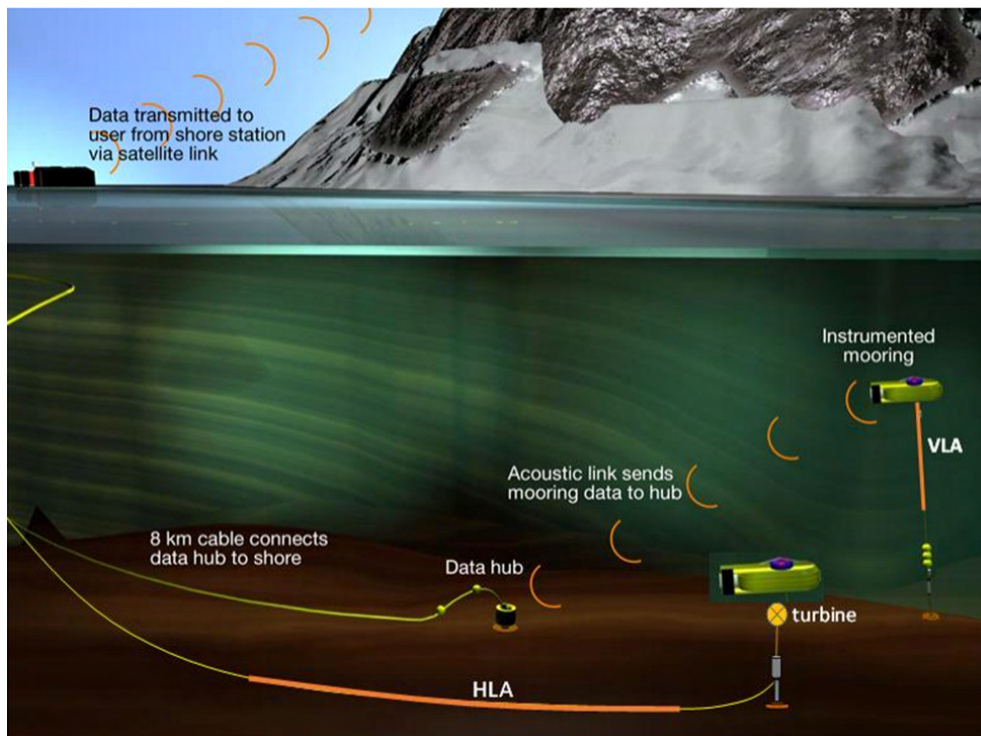
Figure 4.7: VLA and HLA sub-surface mooring concepts connected by underwater cable to an onshore station for transmission of acoustic data to satellite [87].

5 Constellation Design

A satellite constellation is a set of satellites distributed in space that work together to achieve a common objective [88]. Multi-satellite constellations, by their very nature, are expensive systems. Therefore, they are most commonly used to supply valuable world-wide services through the enhanced global coverage capabilities of satellites. These include communications, navigation, and most recently, internet connectivity through the continuing development of the SpaceX Starlink program [88]. Decades of research into constellation design has resulted in no strict rules being established as there exist a wide variety of solutions for any objective [88]. The variety of constellation solutions is best illustrated by the Galileo and BeiDou Global Navigation Satellite Systems (GNSS). The Galileo constellation is comprised of 30 satellites in Medium Earth Orbit (MEO) at an altitude of 23,222 km with 10 satellites distributed evenly across three orbit planes inclined at 56° [89]. Figure 5.1 shows the Galileo constellation.
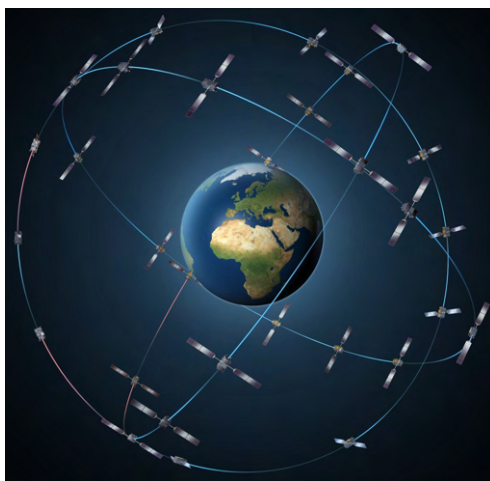
Figure 5.1: Galileo GNSS constellation concept diagram [89].

By contrast, the Chinese GNSS solution BeiDou uses 35 satellites [90]. These satellites are distributed as follows: five in geostationary orbit (GEO), three in inclined geosynchronous orbit (IGSO), each in their own orbital plane inclined at 55°, and 27 satellites in MEO at an altitude of 21,500 km evenly distributed across three orbital planes inclined at 55° [90]. Figure 5.2 shows the BeiDou constellation.
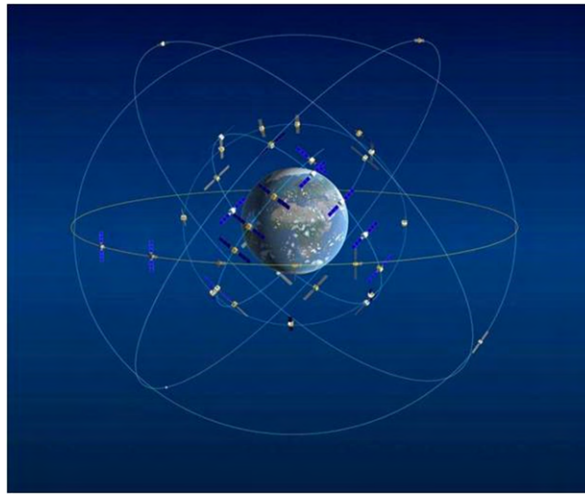
Figure 5.2: Beidou GNSS constellation concept diagram [90].

The concept of constellation variety is extended to LEO where a larger number of satellites is required to achieve continuous coverage of a particular area. The simplest LEO constellation designs make exclusive use of circular orbits in order to avoid the satellites passing through the inner Van Allen Radiation Belt. This region of highly energetic charged particles generally extends from 1,000 km to 12,000 km in altitude but can reach as low as 200 km in the South Atlantic Anomaly during times of increased solar activity [91]. Using circular orbits also allows for link margins to remain unchanged throughout the orbit. This decreases satellite cost and reduces the complexities of the orbital perturbations. Constellations using elliptical orbits such as the Molniya constellation allow for increased capabilities for a particular goal. These constellations however, require a more complex satellite and mission design in order to be able to withstand the more intense radiation environment they encounter throughout their orbits and accommodate the gradual circularization of orbits due to atmospheric drag around perigee [88].

5.1 Walker Constellation

The most common satellite constellation configuration considered for LEO space missions is the Walker constellation [88]. The Walker constellation uses a simple notation to describe the design of a constellation. For this notation, t, represents the total number of satellites in the constellation, p represents the number of orbital planes, f is the relative spacing of satellites in adjacent planes, and s is the number of satellites per plane [88]. The Walker-Delta constellation evenly distributes t satellites across p planes with all planes at the same inclination relative to the equator. The ascending nodes of the orbit planes are distributed evenly around the equator at intervals equal to $\frac{360°}{p}$ and the satellites are evenly distributed around each orbit plane at intervals of $\frac{360°}{s}$ [92]. The principle advantage of the Walker Delta constellation is that adjustments to the inclination of the orbits can change where overlapping coverage of satellites takes place [93]. For example, lowering the inclination of the satellites in a Walker Delta constellation reduces overlapping coverage near the poles while increasing it near the Equator [93]. The main disadvantage of the Walker Delta constellation is the inability to establish consistent inter-satellite links between satellites in different orbital planes as the relative position between satellites is constantly changing [94]. Figure 5.3 shows a Walker Delta constellation diagram.
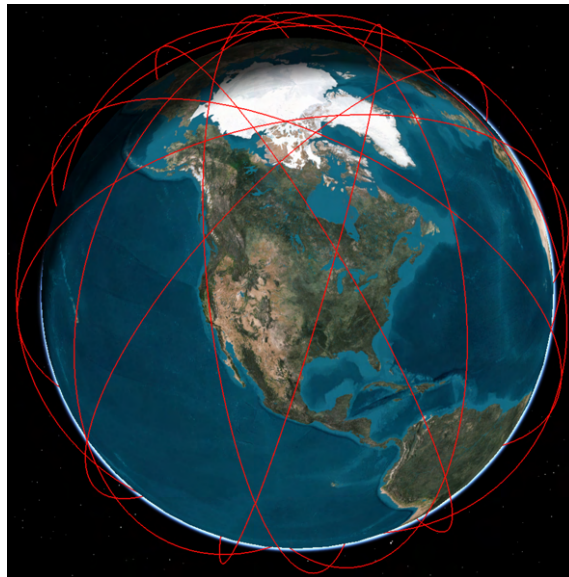
Figure 5.3: STK simulation of a Walker Delta constellation.

The Walker Star constellation is configured such that all satellites move from the South Pole to the North Pole which allows for the establishment of inter-satellite links between satellites in adjacent orbit planes [93]. While the Walker Star constellation is allows for overlapping coverage at the poles, over-crowding of satellites at high latitudes must be considered due to the potential interference of communications on similar frequencies [93]. Furthermore, in order to avoid satellite collisions at the poles, near polar orbits between 80° and 100° are used instead of the perfect 90° polar orbit [94]. Figure 5.4 illustrates a Walker Star constellation configuration.
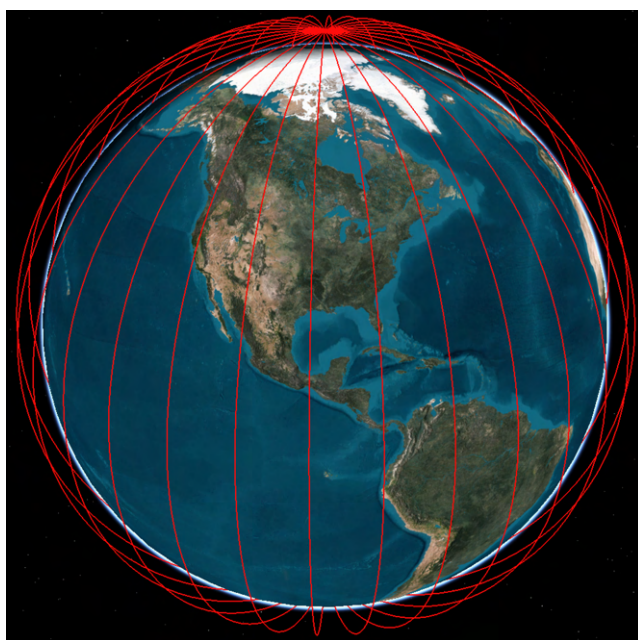
Figure 5.4: STK simulation of a Walker Star constellation.

5.2 Constellation Selection

5.2.1 Constellation Requirements and Constraints

The constellation must maximize coverage of the target areas in order to ensure signals of interest are uplinked with minimal delay. Coverage of ground stations must also be optimized in order to minimize the time taken to downlink the received acoustic data for analysis.

42

Due to the limited transmission power of the hydrophones, the constellation is limited to LEO in order to preserve communications between the hydrophones and satellites.

In order to minimize cost while retaining the required capabilities of the system, CubeSats will be used to populate the constellation. These satellites, made up of standard 10 cm × 10 cm × 10 cm cubes stacked together, are limited in power and are unable to crosslink with geosynchronous satellites to allow near-real time transmission of acoustic data to the ground stations. Therefore, a constellation configuration that allows for inter-plane crosslinks to further minimize data latency should be explored.

5.2.2 Determination of the Optimal Number of Satellites

To identify the optimal constellation configuration for the proposed system, coverage of the target areas detailed in Chapter 4 as well as ground stations in Halifax, Winnipeg, and Victoria must be analysed. Detailed information about the ground stations is presented in Chapter 6.4.1. Uplink of acoustic data only occurs at the target areas while downlink only occurs at the ground stations. The first step is to identify the optimal range for the number of satellites for the constellation configuration. This was done using the AGI Systems Tool Kit (STK) software. For this step, a nominal inclination of 83° and a single satellite per plane at an altitude of 600 km were used. These values were selected with consideration given to the desired area of coverage and the limited transmission power of hydrophones. To make the constellation as cost-effective as possible, one satellite per plane was used in order to be able to determine the minimum number of satellites needed in each configuration to provide robust daily coverage. Establishing a range of the number of satellites required to achieve sufficient coverage of the areas of interest provides insight into what different constellation configurations are possible. All tables containing daily coverage statistics of the considered constellations are found in Appendix A. Table A.1 presents representative daily coverages of all target areas and ground station locations for a range of planes in the Walker Delta configuration. With 16 satellites, the Walker Delta constellation provides 100% daily coverage of four out of five of the selected regions with the least number of satellites while still maintaining competitive coverage values for area E and the ground station locations.

Table A.2 presents representative daily coverages of all target areas and ground station locations for a range of planes in the Walker Star configuration. With 20 satellites, the Walker Star constellation provides the best coverage of the areas of strategic interest and is therefore selected for further consideration.

43

Approaching the 20-satellite configuration, the increases in coverage diminish to the point where adding more satellites to the constellation is no longer worth the increased cost associated with doing so. Therefore, the optimal range of satellites to use in this constellation is between 16 and 20.

5.2.3 Constellation Inclination Analysis

The next step is to determine the optimal inclination for the selected constellation configurations. Table A.3 shows representative daily coverages of all target areas and ground station locations for a range of inclinations for the selected Walker Delta configuration. The 83° inclination for the Walker Delta constellation provides the best compromise between coverage of the strategic areas of interest and coverage of ground stations and, as a result, is selected for further consideration.

Table A.4 shows representative daily coverages of all target areas and ground station locations for a range of inclinations for the selected Walker Star configuration.The 89° inclination for the Walker Star 20-plane constellation provides the best coverage of the strategic areas of interest with only a marginal decline in the daily coverage of ground stations and, as a result, is selected for further consideration.

5.2.4 Constellation Configuration Analysis

The next factor to consider in the design of the satellite constellation is the configuration. For this step, 20 satellites will be used for both Walker Delta and Walker Star configurations in order to make a fair comparison. Inserting satellites into a large number of orbital planes is cost-prohibitive due to the increased number of launches required. Therefore, configurations with a reduced number of orbital planes and more satellites per plane must be considered. Configurations of both Walker Delta and Walker Star constellations with one plane with 20 satellites, two planes with 10 satellites each, 4 planes with 5 satellites each, and 5 planes with 4 satellites each will be considered. Table A.5 presents daily coverages of all target areas and ground stations for the selected Walker Delta constellation configurations. The two-plane configuration of the Walker Delta constellation provides the most comprehensive coverage of all target areas while maintaining competitive coverage of all ground stations. It therefore is selected for further consideration.

Table A.6 presents daily coverages of all target areas and ground stations for the selected Walker Star constellation configurations. The two-plane configuration of the Walker Star constellation provides the most comprehensive

coverage of all target areas while improving the coverage of ground stations by more than 20% per day compared to the optimal Walker Delta configuration. Therefore, the two-plane Walker Star constellation is the configuration of choice for this system.

5.2.5   Parameter Optimization of the Selected Constellation

As the transmission power of hydrophones is limited and the data being collected is of great importance to national security, there is a need to minimize the link margin in order to ensure consistent communications. One way to accomplish this is to minimize the altitude of the satellites in order to reduce space loss as much as possible. Table A.7 presents daily coverages of all target areas and ground stations for the selected constellation configuration for a range of satellite altitudes. A 600 km altitude is the lowest altitude that enables the constellation to achieve 100% daily coverage. The final step in determining the optimal constellation is to determine the minimum number of satellites per plane in the selected configuration that enable 100% daily coverage of all target areas. The previously established optimal range of satellites extended from 16 to 20 in total. As such, the same range of satellites will be considered for this configuration. Table A.8 presents daily coverages of all target areas and ground stations for the selected constellation configuration for a range of satellites per plane.

The minimum number of satellites required to achieve 100% daily coverage of all target areas is 10 satellites per plane. Therefore, the optimal constellation configuration for this system is a two-plane Walker Star constellation with 10 satellites per plane, an 89° inclination, and an altitude of 600 km. This configuration provides the best possible coverage of all target areas and ground stations while minimizing the costs associated with designing, building, and launching numerous satellites. The reduced number of planes allows for a reduction in the number of launches required to position the satellites in the constellation, further reducing costs and mission timelines leading up to on-orbit operations. Figure 5.5 displays the selected constellation configuration along with the strategic areas of interest and ground station locations.
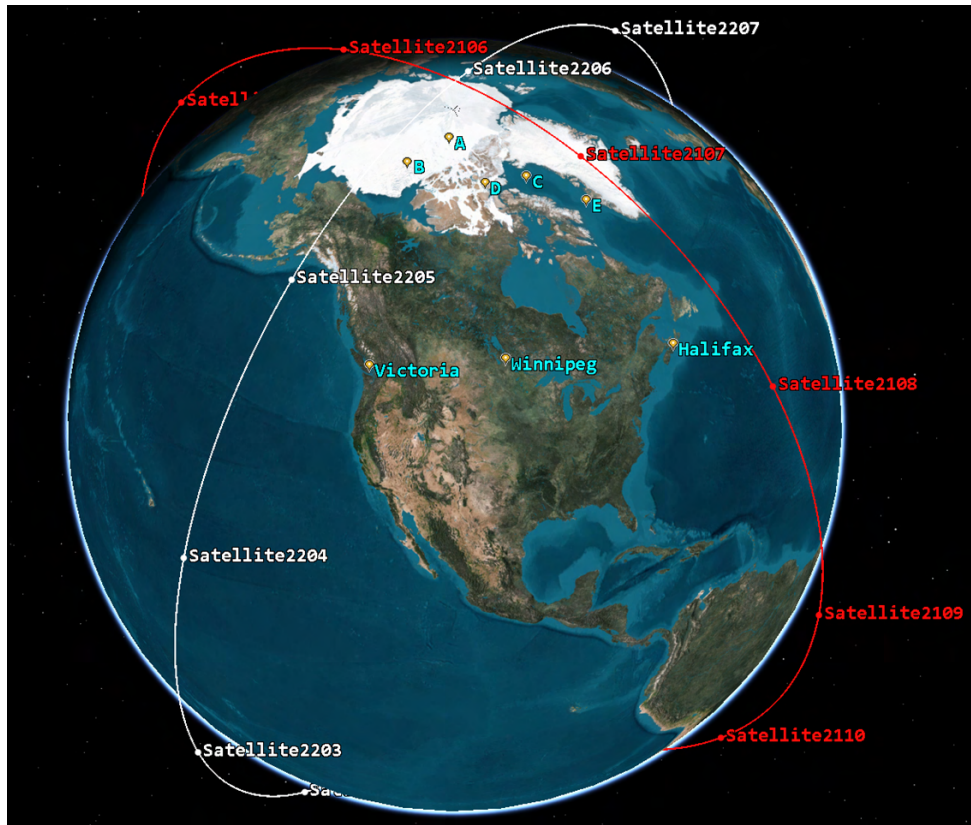
Figure 5.5: STK simulation of the selected Walker Star constellation with strategic areas and ground stations indicated.

The principal limitation with this configuration is data latency. On a descending pass, the satellites are able to downlink the data within minutes of receiving it. On an ascending pass however, the satellites will have to complete nearly an entire orbit before being able to connect to a ground station. This increases the time between reception and downlink to approximately 86 minutes. In order to reduce the data latency for ascending passes, at least four planes of satellites are required in a Walker Delta configuration. Figure 5.6 shows the four-plane configuration of the proposed constellation.

46
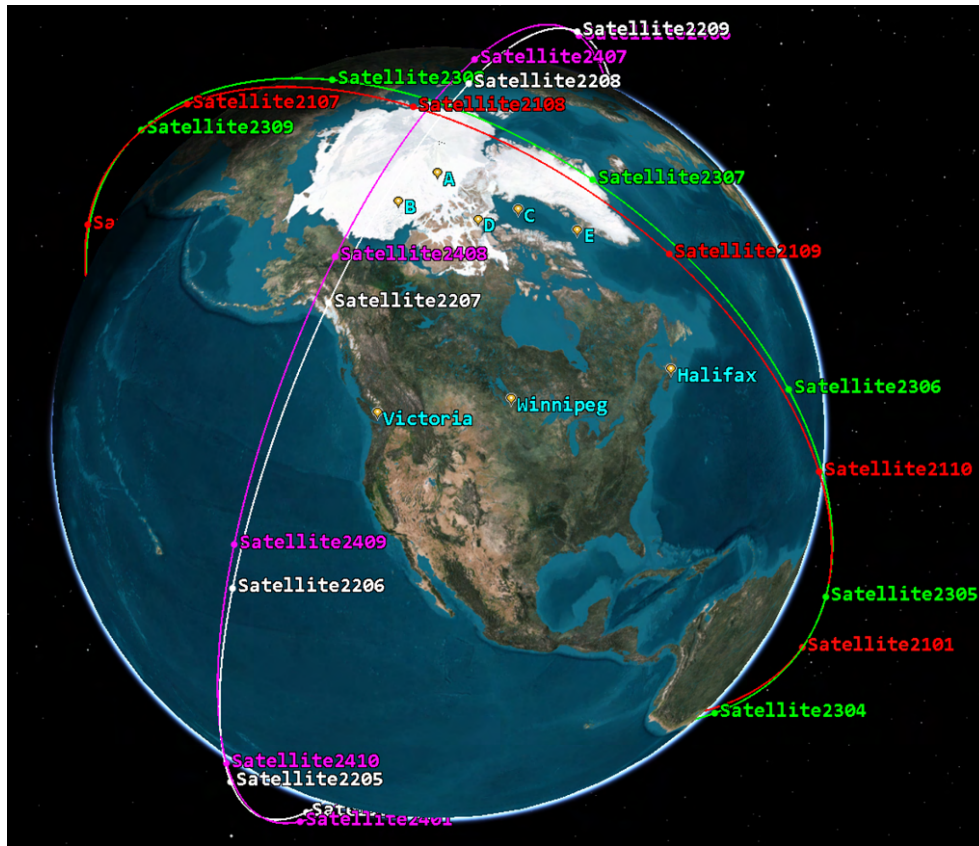
Figure 5.6: STK simulation of the proposed Walker Delta constellation with two more planes of satellites. Strategic areas and ground stations are also indicated.

This configuration facilitates communication between satellites in adjacent planes. Furthermore, within each pair of planes, there is one ascending plane and one descending plane. This doubles the frequency of descending passes while allowing satellites on an ascending pass to crosslink collected data to a satellite on a descending pass. This allows the data to reach the ground station in a similar time frame to a standard descending pass. The limitations of this configuration are increased cost and complexity resulting from the number of satellites being doubled and having to place the satellites into four different orbital planes instead of two.

6 Satellite Design

6.1 Mission Concept

After the placement of hydrophones, the biggest challenge associated with collecting acoustic data in the Arctic is moving the data south to a facility equipped to analyse it. A space-based data relay system in the form of the constellation proposed in Chapter 5 solves this problem. Due to their smaller size, accelerated development to launch timelines, and reduced development and launch costs, CubeSats are an ideal choice for the proposed system. Each individual CubeSat within the proposed constellation will act as a communications relay using a store and forward operations concept where the satellite will receive acoustic data from the hydrophones, store it on board, and then downlink the data once it gets within range of a ground station. The mission concept is summarized in Figure 6.1.
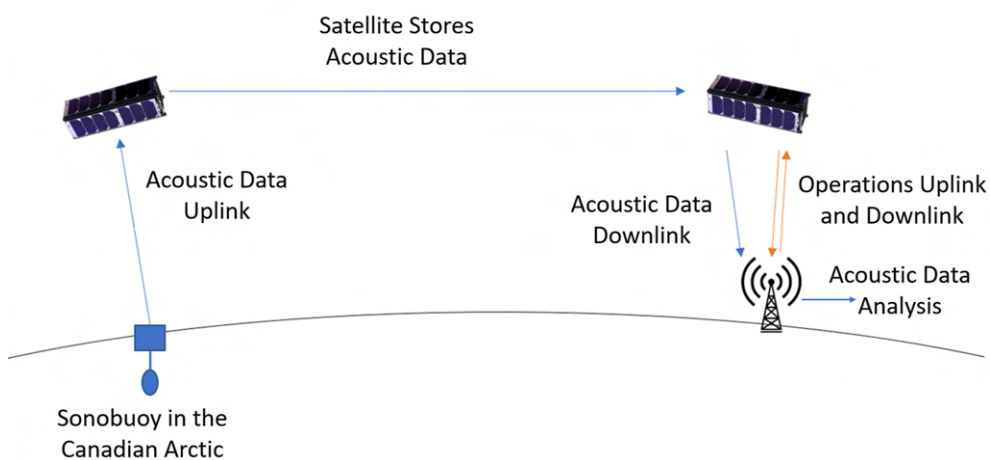
Figure 6.1: Satellite-based data relay operations concept.

6.2 Mission Requirements and Constraints

The satellites must be able to operate at peak power during both daylight and eclipse. Since the primary objective of this system is to relay acoustic data pertaining to the potential location of hostile submarines and surface vessels, it is essential that the satellites are able to perform all essential communications operations in both daylight and eclipse. As such, a robust secondary power system is required to ensure the satellites are able to conduct all necessary operations in eclipse.

The satellites will be 3U (10×10×30 cm) in size in order to remain compatible with available CubeSat deployer systems. Therefore all subsystems must be able to fit within the structure and be powered by a limited number of solar panels distributed over the reduced surface area of the satellite. Rapid acquisition of satellites in orbit must be prioritized due to potential inaccuracies associated with the CubeSat deployment mechanism.

As the satellites are in LEO, they will transition from daylight to eclipse between 14 and 15 times per day. This requires a robust thermal control solution that provides heat for the various components during eclipse and enough protection from heating during daylight to keep the satellite from exceeding the operational temperature range of its components.

To maintain the coverages detailed in Chapter 5, the satellites within the constellation must be kept within a specific phasing of each other and they must also be able to correct for the orbital perturbations present in the LEO environment. The satellites must therefore be equipped with a propulsion system that possesses a high specific impulse (I_{sp}) due to the fuel storage constraints imposed by the small size of the 3U CubeSat platform intended for use. Robust satellite position tracking is also necessary in order to optimize the use of the on-board propulsion system to maintain the satellites within the constellation.

It is required that upon mission completion, CubeSats must be de-orbited within 25 years. The CubeSats will therefore use the on-board propulsion system to accelerate the de-orbit phase of the mission. This means that a certain amount of propellant must be reserved specifically for this phase following the planned 10-year operational lifetime of the satellites.

6.3 Space Segment

6.3.1 Payload

The payload for the satellites is a VHF receiver and antenna tuned to receive from the 130 to 173.5 MHz range used by hydrophones [76]. As there will be multiple hydrophones in close proximity to each other in order to maximize the positional and directional accuracy of the data, a multichannel VHF receiver is required in order to ensure data from each hydrophone can be distinguished. VHF antennas for CubeSats are limited in gain with many capable of achieving a gain between 2 dB and 4 dB [95]. VHF receivers are capable of receiving data rates anywhere from 1.2 kbps to over 30 kbps [96]. Nominal characteristics of VHF antennas and VHF receivers for CubeSats are detailed in Tables 6.1 and 6.2 respectively.

Table 6.1: Nominal parameters of CubeSat VHF receivers based on existing systems [96, 97, 98].

VHF Receiver Nominal Parameters	
Parameter	Value
Frequency Range	140 to 150 MHz
Data Rate	1.2 to >30kbps
Power Consumption	100 to 500 mW

Table 6.2: Nominal parameters of CubeSat VHF antennas based on existing systems [95, 99, 100].

VHF Antenna Nominal Parameters	
Parameter	Value
Frequency Range	>10 MHz Bandwidth within specified frequency range
Gain	0 to 4 dB
Power Consumption	40 mW nominal

To minimize the complexity of the ground-based transmitting system, an isotropic VHF transmitter is assumed. An 8 W transmission power from the ground-based system is assumed based on capabilities from current systems [87]. Using a nominal receiver antenna gain of 3 dB, a data rate of 9.6 kbps, and a frequency of 130 MHz, the link margin is calculated to be 7.0 dB at the minimum elevation angle. For the high end of the hydrophone frequency range

50

at 173.5 MHz, the link margin is calculated to be 4.5 dB. As the minimum required link margin for a reliable satellite relay is 3 dB, this allows for a reduction in transmission power to 3.3 W which results in a link margin of 3.1 dB for a 130 MHz frequency [88]. At 173.5 MHz, the transmission power can be reduced to 5.8 W which results in a link margin of 3.1 dB. A sample calculation of the link margin from a hydrophone to the satellite is found in Appendix B.

6.3.2 Communications

The proposed communications system consists of an S-band transmitter and antenna to downlink payload data as well as telemetry, tracking, and command (TT&C) data. The VHF antenna and VHF receiver will be used to receive command data from the ground station. The S-band and VHF and ground antenna specifications used to determine the link margins for the uplink and downlink are based on similar systems currently in place at RMC and their relevant specifications are presented in Table 6.3.

Table 6.3: Specifications for VHF and S-band ground station antennas similar to those already in place at RMC [101, 102].

Parameter	VHF	S-band
Frequency (MHz)	145.8 to 149.9	2200 to 2450
Gain (dB)	11.5 to 12.3	35.4
Data Rate (kbps)	1.2 to 9.6	9.6 to 115.2
Transmit Power (W)	10	N/A (receive only)

CubeSat S-band transmitters and antennas have a robust space heritage with a range of different systems available for off-the-shelf purchase. CubeSat S-band antennas are capable of achieving gains between 5 and 7 dB and transmitters typically achieve data rates between 56 and 20,000 kbps with transmission powers ranging from 1 to 10 W with the vast majority not exceeding 3 W [100]. Using commercial off-the-shelf (COTS) component specifications detailed alongside the final link margin calculations in Appendix B, the VHF uplink margin was calculated to be 18.2 dB and the S-band downlink margin was calculated to be 7.7 dB.

6.3.3 Navigation

The satellites will be placed into two orbit planes at an inclination of 89° and an altitude of 600 km where they are evenly spaced around the Earth.

The satellites must maintain their phasing in the constellation in order to ensure the coverages of all target areas and ground stations are kept at the values detailed in Chapter 5. Therefore, consistent, precise navigation data throughout the orbit is required for constellation maintenance. In order to achieve successful stationkeeping within a LEO constellation, an in-track position accuracy of 300 to 600 m is required [103]. The payload does not need to be operated when the satellite is not over a target area or a ground station. Precise navigation data is therefore not needed to communicate to the payload when to start operations which means the payload does not need to be considered when determining navigation requirements. Communications to and from the ground station require similar levels of precision in navigation data to payload operations and, as a result, also do not need to be considered when determining navigation requirements. As detailed further in the power section, thrusters will need to fire every third orbit to maintain constellation integrity. The satellites communicate with three dedicated ground stations which will receive position and orbit data from the satellite for constellation monitoring. Navigation data is therefore needed at the ground stations in order for orbit maintenance commands to be uplinked to the satellites.

The most common method of navigation and orbit determination for Cube-Sat missions is done using the classical orbit elements of the satellite, obtained from a two-line element set (TLE). TLEs are not highly accurate and can exhibit position errors up to 2.5 km depending on the time since the previous TLE. The rate at which TLEs are updated compounds this problem as updated orbital elements are made available a limited number of times per day depending on the mission [104]. Doppler Orbitography and Radio-positioning Integrated by Satellite (DORIS) allows for more precise positioning with accuracies better than 10 cm made possible by a worldwide network of 51 ground stations ensuring that a satellite is within range of multiple stations at once [105]. A DORIS receiver consumes between 20 to 26 W and is at least 3.2 U in size, therefore the DORIS system is not feasible for this mission due to the size and power limitations of the satellite [106]. Satellite Laser Ranging is capable of accuracies on the order of cm but cannot act as a standalone system since precision orbit determination is required in order to aim the laser at the satellite [107]. Additionally, to achieve accurate returns, satellites must be fitted with retroreflectors that minimize laser scattering [107]. The Tracking Data Relay Satellite System is capable of determining real-time positions of suitably equipped satellites with an accuracy of 10 m but the geostationary position of the constellation presents coverage limitations for satellites with high inclination orbits which disqualifies it from consideration for this mission [108]. GNSS-based navigation using constellations such as GPS, GLONASS, and

Galileo can achieve up to 10 cm accuracy when used in conjunction through a multi-GNSS receiver [109]. The use of such a receiver also makes it easier to obtain signals from four different satellites which is required to achieve 3-dimensional positional accuracy along with accurate timing [110]. A limitation of this system is that satellites must always be oriented such that the GNSS antenna is pointed up at the GNSS constellations. Horizon Scanner Navigation can achieve positional accuracies of 150 m and can be used for attitude determination [111].

At an altitude of 600 km, the satellites will be exposed to perturbations from Earth oblateness, atmospheric drag, 3rd body effects, and solar radiation pressure [88]. Figure 6.2 illustrates the strength of orbital perturbations for different orbit altitudes.
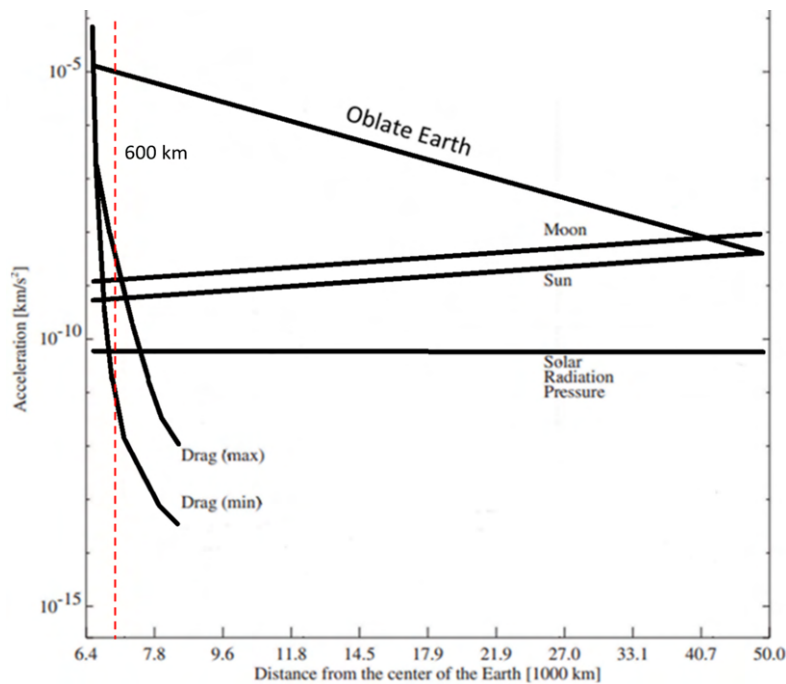
Figure 6.2: Strength of orbital perturbations as a function of altitude with the altitude of the proposed satellites indicated by the dotted red line. Adapted from Montenbruck, Oliver, et al. [112].

From Figure 6.2, it can be seen that the Oblate Earth perturbation is the dominant perturbation by approximately four orders of magnitude [112]. The oblate Earth perturbation induces secular perturbations in the right ascension

of the ascending node (RAAN) [Ω], argument of the perigee (ω), and mean anomaly (M) [113]. The RAAN indicates where the orbit of a satellite intersects the equatorial plane of the Earth while travelling from north to south [113]. The first term expression for the secular oblate Earth perturbation on the RAAN of a satellite is

$$\dot{\Omega} = -\frac{3nR_e^2 J_2}{a^2 (1 - e^2)^2} cos\,(i) \tag{6.1}$$

where n is the mean motion of the satellites in $\frac{orbits}{day}$, R_e is the mean equatorial radius of the Earth (6378.137 km) in km, J_2 is the zonal harmonic coefficient $\left(1.0826269 \times 10^{-3}\right)$, a is the semi-major axis of the orbit in km, e is the eccentricity of the satellite (unitless value between 0 and 1), and i is the inclination of the satellite in degrees [113].

The argument of the perigee is the angle within an orbit measured from the RAAN to the perigee point measured in the direction of travel of the satellite [113]. The first term expression for the secular oblate Earth perturbation on the argument of the perigee of a satellite is

$$\dot{\omega} = \frac{3nR_e^2 J_2}{2a^2 (1 - e^2)^2} \left(4 - 5sin^2\,(i)\right) \tag{6.2}$$

The mean anomaly is the fraction of the period of an elliptical orbit that has passed since the satellite passed the perigee point. It is measured as the angle from the perigee point to the point on a perfectly circular orbit of the same period as the original orbit to where the satellite would have travelled over a given period of time [113]. The first term expression for the secular oblate Earth perturbation on the mean anomaly of a satellite is

$$\dot{M} = \frac{3nR_e^2 J_2}{2a^2 \left(1 - e^{\frac{3}{2}}\right)^2} \left(2 - 3sin^2\,(i)\right) \tag{6.3}$$

In order to maintain robust coverage of the selected target areas by the proposed constellation, the phasing of the satellites within the constellation and their orbit parameters must be strictly maintained. This requires a trajectory control system that is capable of operating semi-autonomously as the number of satellites in the proposed constellation makes solely ground-based trajectory control unrealistic from an operations perspective.

Based on the navigation accuracy, trajectory control requirements, and the limited power supply and space provided by a 3U CubeSat platform, multi-GNSS navigation and low-thrust, high I_{sp} propulsion is the preferred

solution for this mission. The approximately 10 cm accuracy achieved from multi-GNSS navigation is ideal for this mission as precise navigation data is available throughout the orbit. Furthermore, due to the low thrust capabilities of current space-rated CubeSat propulsion systems, the increased accuracy of multi-GNSS navigation data enables the propulsion system to make smaller adjustments which will greatly reduce how long the thrusters must fire to achieve the desired correction [88].

6.3.4 Propulsion

The on-board propulsion system is responsible for satellite stationkeeping and de-orbiting following the end of the mission. Options for propulsion systems for CubeSats are limited due to the low power available and limited amount of space for the propulsion system and fuel. These limitations necessitate a system with high I_{sp} in order to minimize the amount of propellant required. Electrical propulsion systems offer the most promising solution for the propulsion requirements of this mission. Of these systems, electrospray propulsion provides the best combination of high I_{sp} and low input power [100]. At an altitude of 600 km, the estimated delta V for stationkeeping throughout the lifetime of the mission is 600 $\frac{m}{s}$ [88]. The delta V required to reposition the satellite into a lower orbit for de-orbiting at the end of the mission can be calculated with

$$\Delta v_{transfer} = \sqrt{\frac{\mu}{r_L}} \left(\sqrt{\frac{2r_H}{r_L + r_H}} - 1 \right) \tag{6.4}$$

where μ is the gravitational parameter $\left(3.986 \times 10^{14} \frac{m^3}{s^2}\right)$, r_H is the initial orbit radius 6978.1×10^3 m, and r_L is the final orbit radius 6678.1×10^3 m [114]. This results in a transfer delta V of 84.4 $\frac{m}{s}$. This gives a total mission delta V of 684.4 $\frac{m}{s}$. Assuming an electrospray system with an I_{sp} of 1650 s, a spacecraft dry mass of 3 kg, the required propellant mass can be calulated using

$$m_p = m_f \left(\exp \left[\frac{\Delta v}{g_0 I_{sp}} \right] - 1 \right) \tag{6.5}$$

where m_p is the propellant mass in kg, m_f is the mass of the spacecraft exclusive of the propellant, and g_0 is the gravitational constant at the surface of the Earth (9.81 $\frac{m}{s^2}$) [88]. This results in a final propellant mass of 0.13 kg which can be easily accommodated on-board the satellite

6.3.5   Attitude Determination and Control

The attitude of a spacecraft refers to the three-dimensional orientation of the spacecraft with respect to a specified reference frame [115]. Spacecraft attitude is expressed in terms of a roll angle, pitch angle, and yaw angle with roll measured with respect to the X-axis, pitch with respect to the Y-axis, and yaw with respect to the Z-axis [115]. Figure 6.3 visualizes the notation for spacecraft attitude.
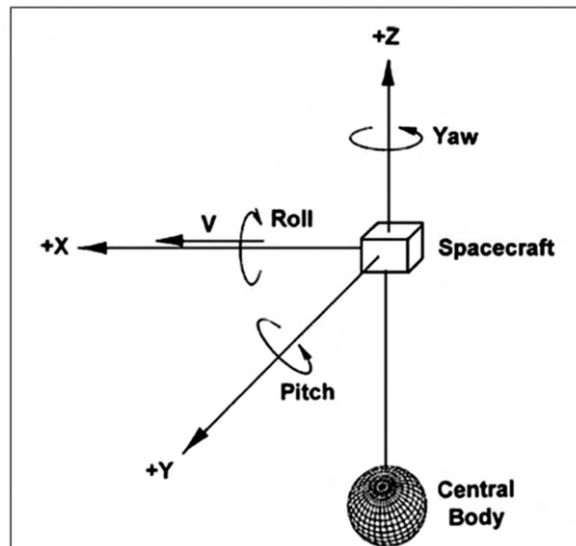
Figure 6.3: Visualization of spacecraft attitude and accompanying notation [115].

In LEO, there are four external disturbance torques that affect the attitude of a spacecraft. These are gravity gradient torque, solar radiation pressure torque, magnetic field torque, and atmospheric drag torque [88]. Gravity gradient torque is caused by the centre of gravity of a spacecraft is not aligned with the centre of mass of the spacecraft with respect to the local vertical [115]. The centre of gravity of an Earth orbiting spacecraft depends on the attitude of the spacecraft relative to the Earth and is generally not the same as the centre of mass [115]. When one of the principal axes is aligned with the local vertical, the centre of gravity is always on that axis and therefore there is no gravity gradient torque [88]. The magnitude of the gravity gradient torque increases as the angle between the principal axes of the spacecraft and the local vertical increases [88]. The expression for the magnitude of gravity gradient

56

torque with respect to the Z principal axis is

$$T_g = \frac{3\mu}{2R^3} |I_z - I_y| \, sin\, (2\theta) \tag{6.6}$$

where T_g is the gravity gradient torque with respect to the X principal axis, μ is the gravitational parameter of the Earth (398,600 $\frac{km^3}{s^2}$), R is the distance from the satellite to the centre of the Earth in m, θ is the angle between the Z principal axis of the spacecraft and the local vertical, and I_y and I_z are the moments of inertia about the Y and Z principal axes respectively in $kg \cdot m^2$.

Solar radiation pressure torque is a result of photons striking a spacecraft in orbit [88]. A first order estimate of the solar radiation pressure torque on a spacecraft can be obtained by assuming a uniform reflectance across the spacecraft and using the following equation

$$T_s = \frac{\Phi}{c} A_s \, (1 + q) \, (cp_m - cm) \, cos\, (\phi) \tag{6.7}$$

where Φ is the average value of the solar constant around Earth (1366 $\frac{W}{m^2}$), c is the speed of light $\left(3 \times 10^8 \, \frac{m}{s}\right)$, A_s is the area of the satellite illuminated by the sun, q is the reflectance factor (unitless value between 0 and 1), ϕ is the angle between the illuminated spacecraft surface and the sun, cp_m is the centre of solar radiation pressure, and cm is the centre of mass of the spacecraft [88].

Magnetic field torque occurs as a result of the residual magnetic moment of a spacecraft being misaligned with the magnetic field of the Earth [115]. To obtain a first order value for the magnetic field torque experienced by a spacecraft, it is possible to approximate the magnetic field of the Earth as a dipole and use the following equation

$$T_M = DB = D \left(\frac{M}{R^3} \lambda \right) \tag{6.8}$$

where T_M is the magnetic field torque, D is the residual dipole moment of the spacecraft in $A \cdot m^2$, B is the strength of the magnetic field in Teslas (T), M is the magnetic moment of the Earth $\left(7.8 \times 10^{15} \, T \cdot m^3\right)$, and λ is a unitless function of magnetic latitude ranging between a value of 1 at the equator and 2 at the poles [88].

Similar to solar radiation pressure, atmospheric drag results from particles in the atmosphere of the Earth striking the spacecraft [115]. Torque from atmospheric drag is created when the centre of the atmospheric pressure is not aligned with the centre of mass of the spacecraft and can be estimated using

$$T_a = \frac{1}{2} \rho C_d A_r V^2 \, (cp_a - cm) \tag{6.9}$$

where T_a is the atmospheric drag torque, ρ is the atmospheric density in $kg \times m^3$, C_d is the drag coefficient of the spacecraft, A_r is the area of the spacecraft exposed to atmospheric drag, also known as the ram area, and cp_a is the centre of aerodynamic pressure on the spacecraft [88].

For this mission, the functions of the attitude determination and control system (ADCS) are to stabilize the spacecraft against external torques, point payload and communications antennas at the ground, and point the spacecraft in the correct direction for orbital maintenance and de-orbiting maneuvers. The function with the most stringent ADCS requirement is the pointing of the spacecraft for orbital maintenance and de-orbiting maneuvers with a required accuracy of approximately $1°$ [116]. Due to the limited space available within a 3U CubeSat platform, an integrated ADCS solution is the best choice for satisfying the ADCS requirements of this mission. Current COTS integrated ADCS systems are capable of achieving pointing accuracies of less than $1°$ and typically integrate star trackers, magnetometers, reaction wheels, and magnetic torquers [100]. This allows the integrated ADCS system to provide highly accurate spacecraft pointing in daylight and eclipse in support of propulsion system operations.

6.3.6   Power

The orbital period and maximum eclipse time were calculated in Appendix C to be 96.7 mins and 35.5 mins respectively. In order to calculate the average power requirements for a typical orbit, average access times for target areas and ground stations must be determined. STK was used to simulate the average access times for all target areas and ground stations based on access durations for all satellites within the constellation throughout a 24-hour period. These values are presented in Table 6.4.

Table 6.4: Average satellite access times for all target areas and ground stations over 24 hours.

Location	Average Access Time (mins)
Target A	12.7
Target B	12.0
Target C	11.4
Target D	11.6
Target E	9.3
Halifax	10.2
Winnipeg	9.8
Victoria	10.2
Average target area access time	11.4
Average ground station access time	10.1

The estimated power budget for the mission is displayed in Table 6.5. The values used are based of off readily available COTS systems and space rated designs.

Table 6.5: Power budget for a typical orbit for the proposed satellites in W.

Component	Cruise	Data Collection	Communications
Propulsion [100]	4	0	0
UHF/VHF Transceiver [96]	0	0.350	0.350
UHF/VHF Antenna [99]	0	0.04	0.04
On-Board Computer[117]	0.4	0.4	0.4
GNSS [118]	0.1	0.1	0.1
Integrated ADCS [119]	1.4	1.4	1.4
S-band Antenna [120]	0	0	2
S-band Transmitter [121]	0	0	2.5
Total	5.9	2.3	6.8
Time/Orbit	75.2/96.7 min	11.4/96.7 min	10.1/96.7 min
Average Power/Orbit	$(75.2/96.7 \cdot 5.9) + (11.4/96.7 \cdot 2.3) + (10.1/96.7 \cdot 6.8) = 5.6$ W		
Orbit Peak Power	6.8 W Communications		
Eclipse Time/Peak Power	35.5 minutes max eclipse/fully operational (Peak Power = 6.8 W)		

The electrospray propulsion system will not operate during periods of data collection or communications. As such, orbit maintenance maneuvers will only be conducted when the satellite is in cruise mode. The thrusters will only fire when corrections are necessary. In order to keep the eccentricity of the orbit to a minimum, thrusters will need to fire every third orbit alternating between apogee and perigee [103]. For example, thrusters will fire at apogee on orbits one, seven, and thirteen and at perigee on orbits four, ten, and sixteen. For conservatism in the solar array and battery sizing process, the electrospray propulsion system power requirements will be fully considered during cruise periods. Figure 6.4 presents power requirements for the satellites for all phases of a typical orbit.
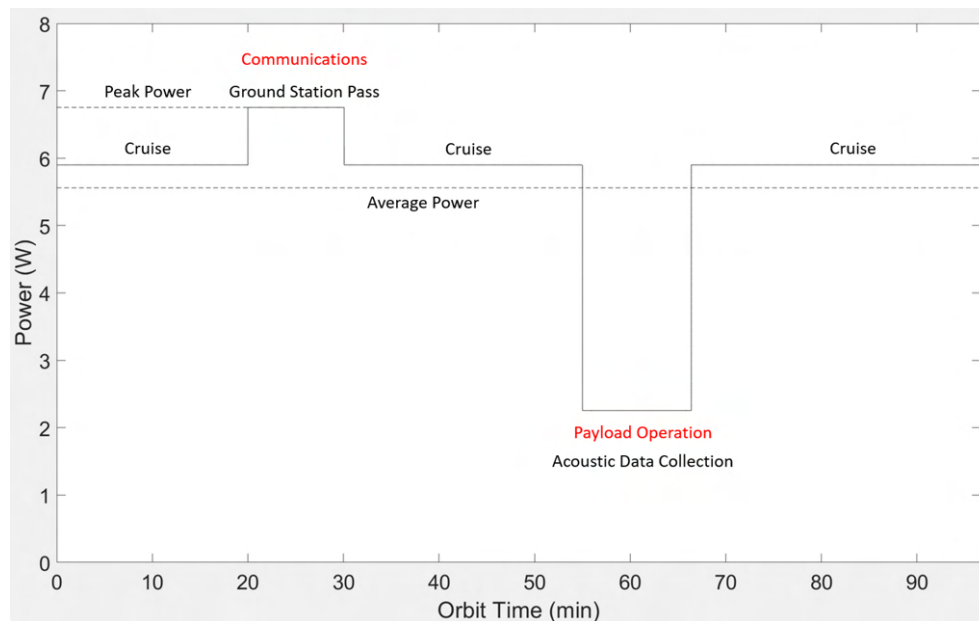
Figure 6.4: Power requirements over one orbit showing average power, peak power, cruise, communications, and payload operation phases.

Using triple junction Gallium arsenide (GaAs) solar cells with an efficiency of 30%, the area of solar cells required to power the satellites is determined to be 479.5 cm^2. This well within the 1300 cm^2 available on the 3U structure [122]. Since the CubeSats must be maintained at a constant orientation in order to continuously receive multi-GNSS navigation data, the area of solar panels exposed to the sun will vary throughout the orbit. Further analysis of

the variation in solar array area exposed to the sun over the course of an orbit will determine whether deployable solar panels are required to meet the power demands of the satellite or whether battery power is required to supplement the solar panels during times of peak power demand. Using specifications for COTS lithium ion batteries, the battery mass required to power the satellite in eclipse is 90.8 g [123]. The calculations for solar cell area and battery mass are found in Appendix C.

6.3.7 Thermal Control

In the 600 km orbit selected for the mission, the satellites will transition between daylight and eclipse an average of 15 times per day. At this altitude, free molecular heating of the spacecraft is minimal [88]. The temperature range the satellites will experience extends from 5.7°C to 118.0°C. This is based on a titanium alloy structure with absorptance and emissivity values of 0.448 and 0.148 respectively [124]. It should be noted that if body-mounted solar panels are selected for use at a more advanced stage of the design process, they will affect the thermal properties of the satellite. Calculations establishing the temperature range for the satellites can be found in Appendix D. Table 6.6 summarizes the temperature ranges for all subsystems.

Table 6.6: Operational temperature ranges for all components on-board the satellites.

Subsystem	Thermal range (°C)
Propulsion [125]	15 to 350
UHF/VHF Transceiver [96]	-15 to 55
UHF/VHF Antenna [99]	-20 to 60
On-Board Computer [117]	-25 to 65
GNSS [118]	-40 to 85
Solar panels [122]	-40 to 125
Integrated ADCS [126]	-45 to 85
S-band Antenna [120]	-20 to 50
S-band Transmitter [121]	-20 to 70

Most systems cannot operate at the upper temperature extreme the satellite will experience. After including a 5 °C buffer, the operational temperature range of the satellite is established to be 20 °C to 45 °C. In order to bring the spacecraft within the operational temperature range, an anodized aluminum coating with an absorptivity of 0.25 and an emissivity of 0.33 will be applied

to the satellite to change the temperature range to -32.4°C to 41.4°C [88]. A network of patch heaters will be installed to provide heat to the spacecraft during eclipse. The heaters will not be operational in daylight. The 28 W power capacity of examined COTS Li-Ion batteries allows for the simultaneous operation of patch heaters and subsystems as the peak power requirement during eclipse only reaches 6.8 W.

6.4 Ground Segment

6.4.1 Ground Stations

As this constellation is responsible for relaying acoustic data as part of a military underwater acoustic surveillance system, minimizing data latency is of paramount importance. To this effect, a dedicated network of ground stations is required. This ensures the satellites will always be able to downlink data that is sensitive to national security without risk of missing a downlink opportunity due to another mission being prioritized for a given pass. Setting up multiple dedicated ground stations is an expensive endeavour but a necessary one as commercial fee for service ground station networks are not an option for handling data pertaining to national security. The locations selected for the proposed ground stations are Halifax, Nova Scotia, Winnipeg, Manitoba, and Victoria, British Colombia. These locations were selected due to their proximity to defence establishments and the lack of overlap in downlink coverage. Halifax contains Canadian Forces Base (CFB) Halifax, the naval base containing the Royal Canadian Navy's Atlantic fleet at and the Acoustic Research Centre. In Winnipeg, CFB Winnipeg, which houses multiple transport and rescue squadrons, provides an effective central operations facility. Lastly in Victoria, CFB Esquimalt is home to the Royal Canadian Navy Pacific fleet. Figure 6.5 displays the number of accesses each ground station is expected to have with the satellites over a given day.
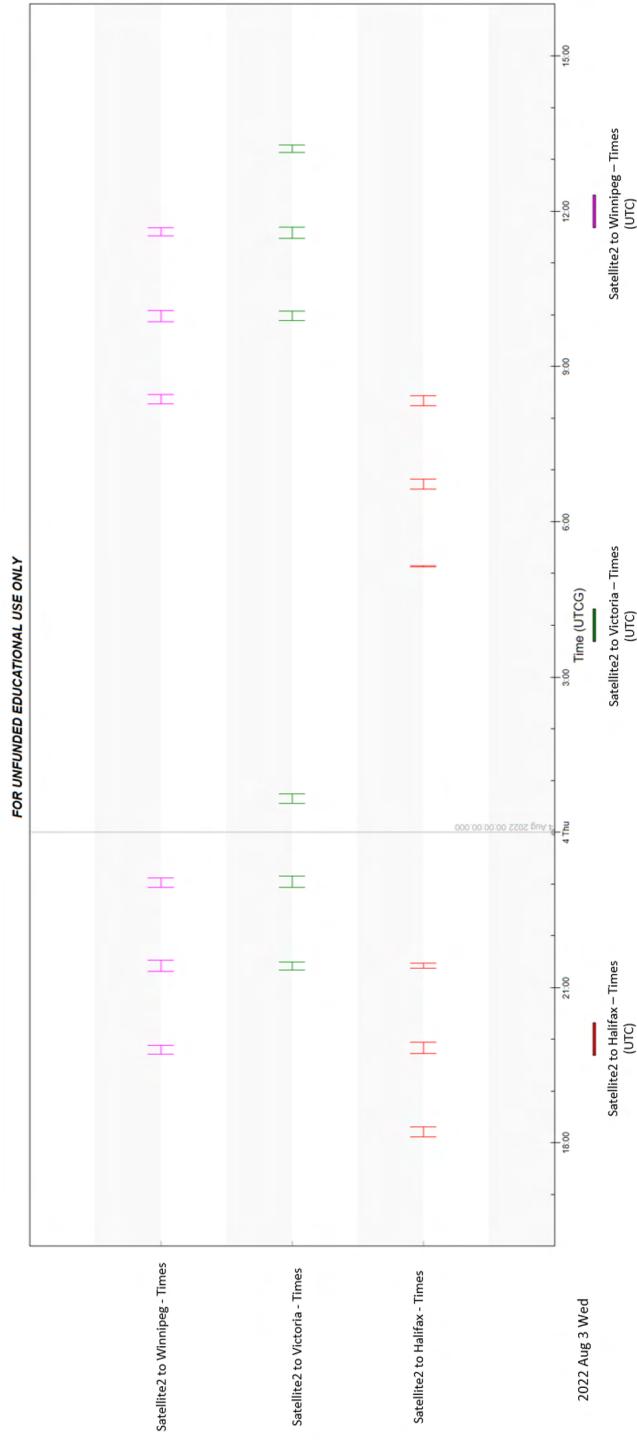
Figure 6.5: Daily accesses of all ground stations from a single satellite within the proposed constellation over a 24-hour period.

64

Using the average access times for the specified target areas and ground stations, as well as nominal data rates for data collection and communications, it is possible to obtain an estimate of how much data can be handled at each phase. Using the longest average access time at Target A of 12.7 mins, an uplink data rate of 9.6 kbps, and assuming at least three hydrophones are deploying in one location to provide triangulation of the position of a contact, the maximum amount of data expected to be collected in a single pass is 21.9 Mb. The shortest average ground station access times of 9.8 mins occur at the Winnipeg ground station. Using a nominal S-band downlink data rate of 56 kbps, the amount of data expected to be downlinked in a single pass is 33.1 Mb. This means that the system will not run the risk of not being able to handle the amount of data it is expected to collect.

6.4.2 Operations

As the proposed system is meant to fulfill a critical surveillance capability for national defence, the acoustic data collected must find its way to the user as quickly as possible. The data will not be processed prior to downlink in order to preserve power on board the satellites and, as a result, will be considered unclassified until analysis is conducted by personnel at the ground stations. Encryption of the data is possible on-board the satellite. In order to ensure that the personnel analyzing the acoustic data are not overwhelmed with volume. The hydrophones will not continuously transmit acoustic data to the satellites. Once a signal exhibiting the characteristics of a target of interest is detected, the hydrophones will uplink the data containing this signal to the satellites which will relay that signal to the ground station for further analysis.

The general pass plan for the satellites is as follows:
1. Communications with satellite established. Satellite downlinks TT&C data via VHF antenna.
2. Satellite downlinks payload data on S-band antenna. Operations personnel analyze payload data prepare commands for the satellite.
3. Commands uplinked to the satellite via VHF antenna.
4. Communications with satellite terminated.

6.5 Audimus

In January 2023, a proposal for an RMC-led proof-of-concept CubeSat mission meant to demonstrate the feasibility of receiving raw acoustic data in space from a hydrophone placed in the Arctic was approved for funding by Defence Research and Development Canada. The mission will receive technical support

from the Canadian Space Agency coincidental with the CubeSats Initiative in Canada for STEM (CUBICS). A mandatory feature of the CUBICS program is that missions must make use of a space-based data relay network. As such, the RMC-led mission, known as Audimus, will forward acoustic data to a space-based LEO satellite network to improve data latency. Audimus will be launched into a sun-synchronous orbit between 400 km and 500 km in altitude. The satellite will be designed to mirror the design proposed in this thesis as this mission is intended to act as an important stepping stone to the full implementation of the proposed system upon mission completion. Figure 6.6 provides an overview of the Audimus mission concept.
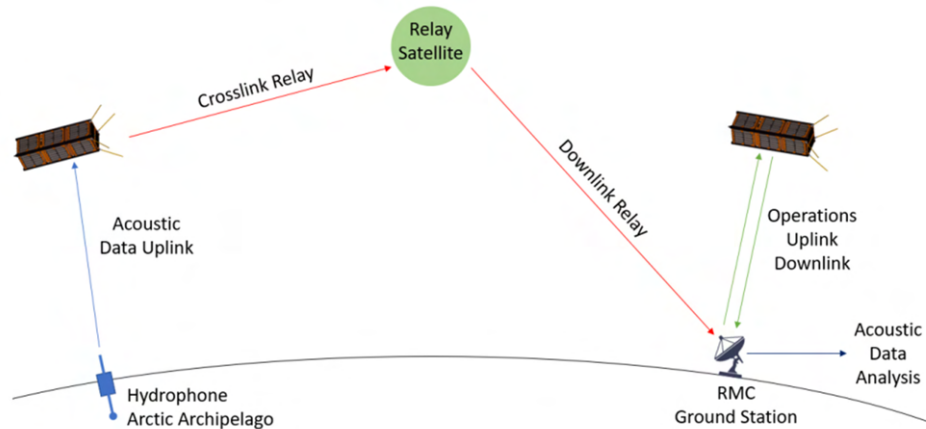
Figure 6.6: Audimus concept of operations.

This mission provides a unique opportunity to involve RMC students directly in the design, development, integration, testing, launching, and operation of a real satellite which allows for the development of highly qualified personnel in the fields of space mission analysis and design, satellite engineering, and mission operations. A secondary objective of the Audimus mission is to test the RMC-developed electrospray propulsion system in orbit. As per the CUBICS agreement, Audimus must be ready for launch three years after the confirmation of funding. Figure 6.7 illustrates the work breakdown structure and proposed development timeline for the Audimus mission.
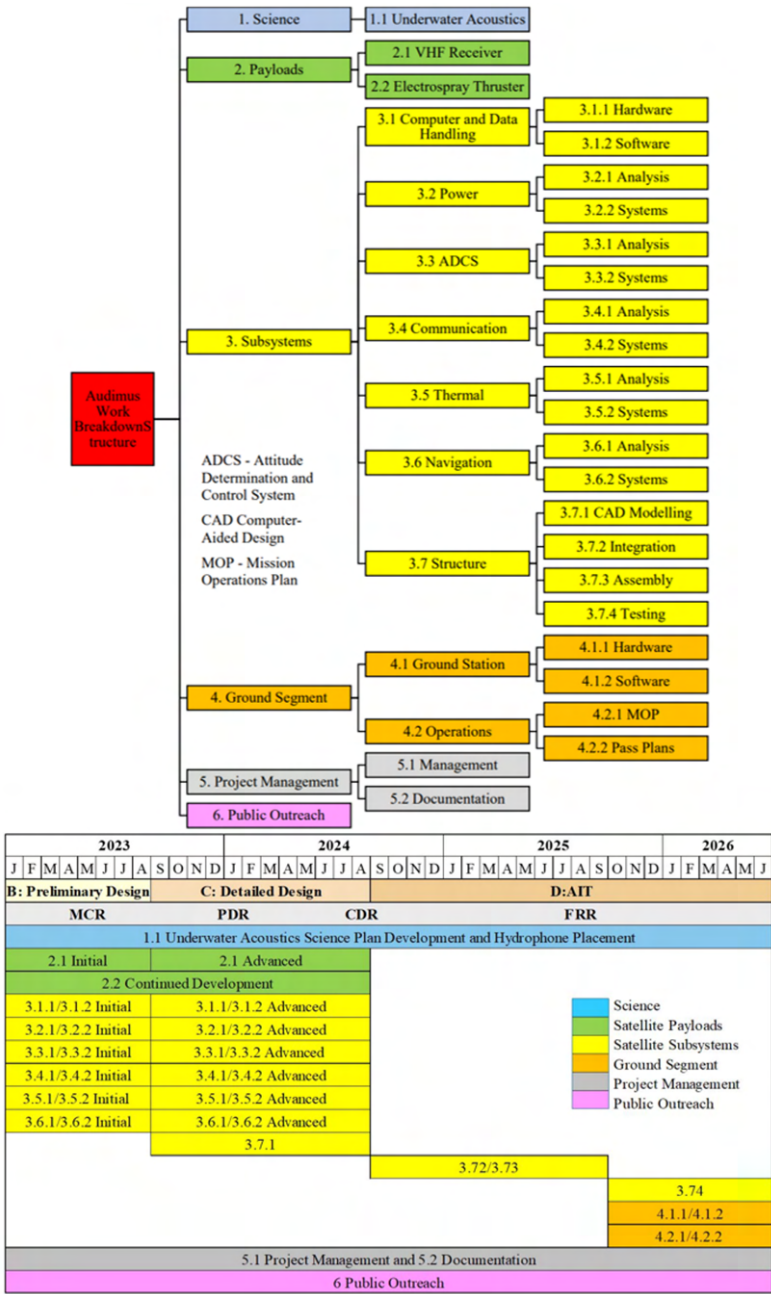
Figure 6.7: Audimus work breakdown structure (top) and proposed timeline for all phases of development (bottom).

7 Conclusion

7.1 Summary

Nuclear proliferation changed the way state security is approached. The importance of alliances to smaller nations with less powerful militaries diminished as the deterrence of nuclear weapons became the most effective way to achieve security. During the Cold War, the threat of Soviet incursions through the Arctic was a chief concern. As such, Arctic security was largely left to the United States and its powerful nuclear submarine fleet. After the end of the Cold War, Canadian plans to purchase a fleet of icebreakers and nuclear submarines for Arctic patrol were scrapped. As a result, Canada's monitoring capabilities are not sufficient to provide adequate situational awareness in the Arctic environment. Given the unpredictable geopolitical climate of the present day, the need for persistent monitoring of the Arctic continues to grow for Canada.

Compounding the problem of a lack of military infrastructure designed for service in the Arctic are the rapid environmental changes taking place as a result of climate change and Arctic amplification. Sea ice extent in the Arctic has declined by more than 50% since consistent satellite observations of the region began in 1979. This makes transits under the ice easier for modern day submarines which have greater endurance, are harder to detect, and have more advanced sonar and weapons systems. The accelerated melting of sea ice is also increasing the proportion of first-year ice in the Arctic which is leading to higher net sea ice exports through Fram Strait, Nares Strait, and the CAA.

The underwater acoustic environment in the Arctic is different from that of temperate oceans primarily due to ice cover. The presence of sea ice prevents near surface mixing resulting from interactions between the ocean surface and the wind and near surface heating from the sun. This results in a monotonically increasing sound speed profile which continuously refracts sound waves upwards known as half-channel propagation. The variability of sea ice in the Arctic makes acoustic modelling in the region particularly challenging.

Canada does not have access to the range-dependent version of the OASES model which is considered to be the standard for acoustic propagation. The Bellhop model presents a suitable middle ground that able to converge for both rough and smooth ice scenarios but overestimates propagation losses, particularly at longer ranges.

Five areas of interest have been identified for acoustic surveillance. Canada Basin and the Beaufort sea on the west coast of the CAA, the Northwest Passage around Gascoyne Inlet, northern Baffin Bay, and Davis Strait. Surveillance of these areas allows for early detection of any surface or sub-surface vessel attempting to enter Canadian waters. Detection ranges in these areas vary depending on the season but typically range from 7 km to over 100 km. In Canada Basin and the Beaufort Sea, year-round multi-year ice coverage necessitates the use of an ice-tethered VLA. In Baffin Bay and Davis Strait, highly-variable ice coverage throughout the year requires a drifting buoy capable of being frozen into the ice during winter. Lastly, the shallow waters, strong currents, and mobile ice packs in the Northwest Passage demand that underwater moorings connected via cable to a surface station be used.

Due to the limited transmission power of hydrophones, options for satellite constellations are limited to LEO. A two-plane Walker Star constellation at an altitude of 600 km with 10 satellites per plane at an inclination of 89° achieves 100% coverage of the target areas while optimizing ground station coverage with the least amount of satellites. The benefits of this configuration is reduced development and launch costs and simplicity of implementation due to there only being two orbital planes to place the satellites into. The main limitation with this constellation is data latency on ascending passes as the satellites will need to complete nearly an entire orbit before being able to access a ground station. By doubling the number of planes, converting to a Walker Delta configuration, and retaining the original orbital elements, the number of descending passes is doubled. Furthermore, crosslinks between satellites in adjacent planes can be established which reduces data latency for the entire constellation to under 10 minutes. The drawback of this configuration is the increased costs associated with building and launching twice the number of satellites into four different orbital planes.

CubeSats provide a capable low-cost solution for this system. The proposed satellites will be 3U in size. A VHF antenna and receiver will be used to receive acoustic data from the hydrophones in the Arctic and to receive commands from the ground station. An S-band antenna and transmitter will be used to downlink TT&C data and acoustic data to the ground station. Multi-GNSS navigation will be used to determine the position of the satellites. Navigation data will be used at the ground station to instruct the satellites

when to conduct orbit maintenance maneuvers. An on-board propulsion system is required to maintain constellation integrity. An electrospray propulsion system will be used to accomplish this. The estimated delta-V for this mission is 684.4 $\frac{m}{s}$ which requires 0.13 kg of propellant. The on-board ADCS will consist of an integrated ADCS capable of providing fine pointing in daylight and eclipse. The area of solar panels required to power the satellites is 479.5 cm^2 and the mass of Li-ion batteries required to power the satellites in eclipse is 90.8 g. Thermal control is accomplished by applying an anodized aluminum coating with an absorptivity of 0.25 and an emissivity of 0.33 and a network of patch heaters to be used in eclipse. Ground stations will be located in Halifax, Winnipeg, and Victoria due to their proximity to national defence installations and the minimal overlap in downlink coverage between locations.

7.2 Future Work and Recommendations

The Audimus mission seeks to demonstrate the feasibility of transmitting acoustic data from a hydrophone in the Arctic to a LEO CubeSat. This mission is currently in the mission concept review phase with the detailed design and analysis of all subsystems still required. For instance, determining whether deployable solar panels are required in order to meet the power demands of the satellite in daylight and how the solar panel material affects the temperature range of the satellite. This will happen in the preliminary design review and critical design review phases. As Audimus does not seek to demonstrate any new technology, detailed research into novel subsystem capabilities to accomplish the mission is not required.

Once the feasibility of data uplink between a hydrophone and a LEO satellite has been confirmed. It is recommended that a system architecture consisting of hydrophones deployed in the strategic areas detailed in Chapter 4 and a constellation of satellites with the architectures presented in Chapter 5 be implemented as part of the new NORAD modernization program. Further trade-off analysis between data latency and system costs must be conducted.

Bibliography

[1] Allan, J., *Sovereign Statehood*, London: Allen and Unwin, 1986.

[2] Lovett, J., Churchill, R. R., and Lowe, A. V., "The Law of the Sea," *Environment and Development Economics*, Vol. 7, No. 1, 2002, pp. 191–196.

[3] Huebert, R. N., *Canadian Arctic sovereignty and security in a transforming circumpolar world*, Canadian International Council Toronto, 2009.

[4] Carnaghan, M. and Goody, A., *Canadian Arctic Sovereignty*, Parliamentary Information and Research Service Ottawa, 2006.

[5] Baylis, J., Wirtz, J. J., and Johnson, J. L., *Strategy in the contemporary world*, Oxford University Press, 2022.

[6] Collins, A., *Contemporary security studies*, Oxford university press, 2022.

[7] *Challenge and Commitment: A Defence Policy for Canada*, International Specialized Book Service Incorporated, 1987.

[8] "Naval Surveillance Radar SCANTER 6002," https://www.terma.com/media/44hbhzbi/terma-scanter-6002-a4-v7-low.pdf, 2022.

[9] "Harry DeWolf-Class Arctic and Offshore Patrol Vessels," https://www.canada.ca/content/dam/rcn-mrc/documents/ships/aopv-fact-sheet-2022.pdf, 2022.

[10] Box, J. E., Colgan, W. T., Christensen, T. R., Schmidt, N. M., Lund, M., Parmentier, F.-J. W., Brown, R., Bhatt, U. S., Euskirchen, E. S., Romanovsky, V. E., et al., "Key indicators of Arctic climate change: 1971–2017," *Environmental Research Letters*, Vol. 14, No. 4, 2019, pp. 045010.

[11] Yadav, J., Kumar, A., and Mohan, R., "Dramatic decline of Arctic sea ice linked to global warming," *Natural Hazards*, Vol. 103, 2020, pp. 2617–2621.

[12] Francis, J. A. and Wu, B., "Why has no new record-minimum Arctic sea-ice extent occurred since September 2012?" *Environmental research letters*, Vol. 15, No. 11, 2020, pp. 114034.

[13] Hutt, D., "An overview of Arctic Ocean acoustics," *AIP Conference Proceedings*, Vol. 1495, American Institute of Physics, 2012, pp. 56–68.

[14] "NOAA Arctic Sea Ice Decline Record," https://nsidc.org/arcticseaicenews/, 2022, Accessed 2023-01-03.

[15] Zhang, Y. G., Pagani, M., Liu, Z., Bohaty, S. M., and DeConto, R., "A 40-million-year history of atmospheric CO_2," *Philosophical Transactions of the Royal Society A: Mathematical, Physical and Engineering Sciences*, Vol. 371, No. 2001, 2013, pp. 20130096.

[16] "Mauna Loa CO_2 Record," https://gml.noaa.gov/ccgg/trends/, 2023, Accessed 2023-01-04.

[17] Bekryaev, R. V., Polyakov, I. V., and Alexeev, V. A., "Role of polar amplification in long-term surface air temperature variations and modern Arctic warming," *Journal of Climate*, Vol. 23, No. 14, 2010, pp. 3888–3906.

[18] Perovich, D. K., Light, B., Eicken, H., Jones, K. F., Runciman, K., and Nghiem, S. V., "Increasing solar heating of the Arctic Ocean and adjacent seas, 1979–2005: Attribution and role in the ice-albedo feedback," *Geophysical Research Letters*, Vol. 34, No. 19, 2007.

[19] Walter, K., Chanton, J., Chapin Iii, F., Schuur, E., and Zimov, S., "Methane production and bubble emissions from Arctic lakes: Isotopic implications for source pathways and ages," *Journal of Geophysical Research: Biogeosciences*, Vol. 113, No. G3, 2008.

[20] Natali, S. M., Watts, J. D., Rogers, B. M., Potter, S., Ludwig, S. M., Selbmann, A.-K., Sullivan, P. F., Abbott, B. W., Arndt, K. A., Birch, L., et al., "Large loss of CO_2 in winter observed across the northern permafrost region," *Nature Climate Change*, Vol. 9, No. 11, 2019, pp. 852–857.

[21] Dai, A., Luo, D., Song, M., and Liu, J., "Arctic amplification is caused by sea-ice loss under increasing CO_2," *Nature communications*, Vol. 10, No. 1, 2019, pp. 121.

[22] Smedsrud, L. H., Halvorsen, M. H., Stroeve, J. C., Zhang, R., and Kloster, K., "Fram Strait sea ice export variability and September Arctic sea ice extent over the last 80 years," *The Cryosphere*, Vol. 11, No. 1, 2017, pp. 65–79.

[23] Wang, Q., Ricker, R., and Mu, L., "Arctic sea ice decline preconditions events of anomalously low sea ice volume export through Fram Strait in the early 21st century," *Journal of Geophysical Research: Oceans*, Vol. 126, No. 2, 2021, pp. e2020JC016607.

[24] Moore, G., Howell, S., Brady, M., Xu, X., and McNeil, K., "Anomalous collapses of Nares Strait ice arches leads to enhanced export of Arctic sea ice," *Nature communications*, Vol. 12, No. 1, 2021, pp. 1.

[25] Moore, G., Schweiger, A., Zhang, J., and Steele, M., "Spatiotemporal variability of sea ice in the Arctic's last ice area," *Geophysical Research Letters*, Vol. 46, No. 20, 2019, pp. 11237–11243.

[26] Howell, S. E. and Brady, M., "The dynamic response of sea ice to warming in the Canadian Arctic Archipelago," *Geophysical Research Letters*, Vol. 46, No. 22, 2019, pp. 13119–13125.

[27] Lebrun, M., Vancoppenolle, M., Madec, G., and Massonnet, F., "Arctic sea-ice-free season projected to extend into autumn," *The Cryosphere*, Vol. 13, No. 1, 2019, pp. 79–96.

[28] Pizzolato, L., Howell, S. E., Dawson, J., Laliberté, F., and Copland, L., "The influence of declining sea ice on shipping activity in the Canadian Arctic," *Geophysical Research Letters*, Vol. 43, No. 23, 2016, pp. 12–146.

[29] Kwok, R., "Arctic sea ice thickness, volume, and multiyear ice coverage: losses and coupled variability (1958–2018)," *Environmental Research Letters*, Vol. 13, No. 10, 2018, pp. 105005.

[30] Malmstrom, R. R., Straza, T. R., Cottrell, M. T., and Kirchman, D. L., "Diversity, abundance, and biomass production of bacterial groups in the western Arctic Ocean," *Aquatic microbial ecology*, Vol. 47, No. 1, 2007, pp. 45–55.

[31] Chapman, R. and Scott, H., "Backscattering strengths of sea ice," *The Journal of the Acoustical Society of America*, Vol. 39, No. 6, 1966, pp. 1191–1193.

[32] "Canada Defence Policy," https://www.canada.ca/en/department-national-defence/corporate/reports-publications/canada-defence-policy.html, 2019, Accessed 2023-01-14.

[33] Jakobsson, M., "Hypsometry and volume of the Arctic Ocean and its constituent seas," *Geochemistry, Geophysics, Geosystems*, Vol. 3, No. 5, 2002, pp. 1–18.

[34] Jakobsson, M., Mayer, L., and Monahan, D., "Arctic Ocean bathymetry: A necessary geospatial framework," *Arctic*, 2015, pp. 41–47.

[35] Jakobsson, M., Mayer, L., Coakley, B., Dowdeswell, J. A., Forbes, S., Fridman, B., Hodnesdal, H., Noormets, R., Pedersen, R., Rebesco, M., et al., "The international bathymetric chart of the Arctic Ocean (IB-CAO) version 3.0," *Geophysical Research Letters*, Vol. 39, No. 12, 2012.

[36] Cochran, J. R., Edwards, M. H., and Coakley, B. J., "Morphology and structure of the Lomonosov ridge, Arctic Ocean," *Geochemistry, Geophysics, Geosystems*, Vol. 7, No. 5, 2006.

[37] Chiu, P.-Y., Chao, W.-S., Gyllencreutz, R., Jakobsson, M., Li, H.-C., Löwemark, L., and O'Regan, M., "New constraints on Arctic Ocean Mn stratigraphy from radiocarbon dating on planktonic foraminifera," *Quaternary International*, Vol. 447, 2017, pp. 13–26.

[38] Chernykh, A. and Krylov, A., "Sedimentogenesis in the Amundsen Basin from geophysical and drilling evidence on Lomonosov Ridge," *Doklady Earth Sciences*, Vol. 440, " /", 2011, pp. 1372–1376.

[39] Døssing, A., Jackson, H. R., Matzka, J., Einarsson, I., Rasmussen, T. M., Olesen, A. V., and Brozena, J., "On the origin of the Amerasia Basin and the High Arctic Large Igneous Province—results of new aeromagnetic data," *Earth and Planetary Science Letters*, Vol. 363, 2013, pp. 219–230.

[40] Sirevaag, A., de La Rosa, S., Fer, I., Nicolaus, M., Tjernström, M., and McPhee, M., "Mixing, heat fluxes and heat content evolution of the Arctic Ocean mixed layer," *Ocean Science*, Vol. 7, No. 3, 2011, pp. 335–349.

[41] Rudels, B., "Arctic Ocean circulation, processes and water masses: A description of observations and ideas with focus on the period prior to the International Polar Year 2007–2009," *Progress in Oceanography*, Vol. 132, 2015, pp. 22–67.

[42] Aagaard, K., Coachman, L., and Carmack, E., "On the halocline of the Arctic Ocean," *Deep Sea Research Part A. Oceanographic Research Papers*, Vol. 28, No. 6, 1981, pp. 529–545.

[43] Spall, M. A., "On the circulation of Atlantic Water in the Arctic Ocean," *Journal of Physical Oceanography*, Vol. 43, No. 11, 2013, pp. 2352–2371.

[44] Grigor, J., *Ecology and physiology of chaetognaths (semi-gelatinous zooplankton) in Arctic waters*, Ph.D. thesis, Université Laval, 2017.

[45] Kipp, L. E., McManus, J. F., and Kienast, M., "Radioisotope constraints of Arctic deep water export to the North Atlantic," *Nature Communications*, Vol. 12, No. 1, 2021, pp. 3658.

[46] Jungblut, S., Liebich, V., and Bode, M., *YOUMARES 8–Oceans Across Boundaries: Learning from each other: Proceedings of the 2017 conference for YOUng MARine RESearchers in Kiel, Germany*, Springer Nature, 2018.

[47] Armitage, T. W., Bacon, S., Ridout, A. L., Petty, A. A., Wolbach, S., and Tsamados, M., "Arctic Ocean surface geostrophic circulation 2003–2014," *The Cryosphere*, Vol. 11, No. 4, 2017, pp. 1767–1780.

[48] Jensen, F. B., Kuperman, W. A., Porter, M. B., Schmidt, H., and Tolstoy, A., *Computational ocean acoustics*, Vol. 2011, Springer, 2011.

[49] Medwin, H., "Speed of sound in water: A simple equation for realistic parameters," *The Journal of the Acoustical Society of America*, Vol. 58, No. 6, 1975, pp. 1318–1319.

[50] Khan, M. W., Zhou, Y., and Xu, G., "Modeling of acoustic propagation channel in underwater wireless sensor networks," *The 2014 2nd International Conference on Systems and Informatics (ICSAI 2014)*, IEEE, 2014, pp. 586–590.

[51] Johannson, A. T., *Parametric modelling of cetacean calls*, Ph.D. thesis, University of Southampton, 2004.

[52] Schroeder, M., Rossing, T. D., Dunn, F., Hartmann, W., Campbell, D., and Fletcher, N., "Springer handbook of acoustics," 2007.

[53] Urick, R. J., "Principles of underwater sound-2," 1975.

[54] Neighbors III, T., "Absorption of Sound in Seawater," *Applied Underwater Acoustics*, Elsevier, 2017, pp. 273–295.

[55] Stojanovic, M., "Underwater acoustic communications," *Proceedings of Electro/International 1995*, IEEE, 1995, pp. 435–440.

[56] Duan, R., Yang, K.-D., and Ma, Y.-L., "Investigation of long-range sound propagation in surface ducts," *Chinese Physics B*, Vol. 22, No. 12, 2013, pp. 124301.

[57] Nguyen, S. T., Cayirci, E., Yan, L., and Rong, C., "A shadow zone aware routing protocol for acoustic underwater sensor networks," *IEEE Communications Letters*, Vol. 13, No. 5, 2009, pp. 366–368.

[58] "Ray Paths," https://man.fas.org/dod-101/navy/docs/es310/SNR_PROP/snr_prop.htm, 1998, Accessed 2023-01-17.

[59] Lawrence, M., Bell, M., and Prenc, S., "Acoustic propagation by bottom bounce mode to the north east of Australia," Tech. rep., Defence Science and Technology Organisation Canberra (Australia), 1994.

[60] Vadov, R., "On the Predictability of the Positions of the Convergence Zones in the Ocean." *Acoustical Physics*, Vol. 51, No. 3, 2005.

[61] Prior, M. K., Meless, O., Bittner, P., and Sugioka, H., "Long-range detection and location of shallow underwater explosions using deep-sound-channel hydrophones," *IEEE Journal of Oceanic Engineering*, Vol. 36, No. 4, 2011, pp. 703–715.

[62] Alexander, P., Duncan, A., and Bose, N., "Modelling sound propagation under ice using the Ocean Acoustics Library's Acoustic Toolbox," *Proceedings of the Acoustical Society of Australia*, 2012, pp. 1–7.

[63] Worcester, P. F., Dzieciuch, M. A., and Sagen, H., "Ocean acoustics in the rapidly changing Arctic," *Acoust. Today*, Vol. 16, No. 1, 2020, pp. 55–64.

[64] Diachok, O. I., "Effects of sea-ice ridges on sound propagation in the Arctic Ocean," *The Journal of the Acoustical Society of America*, Vol. 59, No. 5, 1976, pp. 1110–1120.

[65] Mikhalevsky, P., "Acoustics Arctic," 2001.

[66] Freitag, L., Ball, K., Partan, J., Koski, P., and Singh, S., "Long range acoustic communications and navigation in the Arctic," *OCEANS 2015-MTS/IEEE Washington*, IEEE, 2015, pp. 1–5.

[67] Duda, T. F., "Acoustic signal and noise changes in the Beaufort Sea Pacific Water duct under anticipated future acidification of Arctic Ocean waters," *The Journal of the Acoustical Society of America*, Vol. 142, No. 4, 2017, pp. 1926–1933.

[68] Merz, S., Kinns, R., and Kessissoglou, N., "Structural and acoustic responses of a submarine hull due to propeller forces," *Journal of sound and vibration*, Vol. 325, No. 1-2, 2009, pp. 266–286.

[69] Ellis, D. D., "A two-ended shooting technique for calculating normal modes in underwater acoustic propagation," Tech. rep., Defence Research Establishment Atlantic Dartmouth (Nova Scotia), 1985.

[70] Wang, L., Heaney, K., Pangerc, T., Theobald, P., Robinson, S., and Ainslie, M., "Review of underwater acoustic propagation models." 2014.

[71] Porter, M. B. and Bucker, H. P., "Gaussian beam tracing for computing ocean acoustic fields," *The Journal of the Acoustical Society of America*, Vol. 82, No. 4, 1987, pp. 1349–1359.

[72] Pecknold, S. and Binder, C., "A Comparison of Acoustic Propagation Models for Canadian Arctic Underwater Sentinel Experimentation (CAUSE)," Tech. rep., Defence Research and Development Canada, 2020.

[73] Cook, E., Barclay, D., and Richards, C., "Ambient noise in the Canadian Arctic," *Governance of Arctic Shipping*, 2020, pp. 105.

[74] Jansen, E. and de Jong, C., "Experimental assessment of underwater acoustic source levels of different ship types," *IEEE Journal of Oceanic Engineering*, Vol. 42, No. 2, 2017, pp. 439–448.

[75] Holler, R. A., "The evolution of the sonobuoy from World War II to the Cold War," Tech. rep., NAVMAR APPLIED SCIENCES CORP WARMINSTER PA, 2014.

[76] "WinRadio WR-G39WSBe Sonobuoy Telemetry Receiver," https://www.winradio.com/home/g39wsbe.htm, 2022, Accessed 2023-01-02.

[77] Salamon, R., "Directional sonobuoy system for detection of submarines," *Hydroacoustics*, Vol. 7, 2004, pp. 195–208.

[78] gu Lee, Y., "Depth estimation of an underwater target using DIFAR sonobuoy," *The Journal of the Acoustical Society of Korea*, Vol. 38, No. 3, 2019, pp. 302–307.

[79] "Spring 2015 geobuoy comparison trial," https://www.canada.ca/en/defence-research-development/news/articles/spring-2015-geobuoy-comparison-trial.html, 2015, Accessed 2023-02-04.

[80] Hines, P., Deveau, T., Hamilton, J., Kessel, R., Martin, S., and Nams, D., "Arctic Acoustic Propagation Projections to 2040," Tech. rep., JASCO Applied Sciences, 2020.

[81] Babb, D. G., Galley, R. J., Howell, S. E., Landy, J. C., Stroeve, J. C., and Barber, D. G., "Increasing Multiyear Sea Ice Loss in the Beaufort Sea: A New Export Pathway for the Diminishing Multiyear Ice Cover of the Arctic Ocean," *Geophysical Research Letters*, Vol. 49, No. 9, 2022, pp. e2021GL097595.

[82] Vincent, R., "An Assessment of the Lancaster Sound Polynya Using Satellite Data 1979 to 2022," *Remote Sensing*, Vol. 15, No. 4, 2023, pp. 954.

[83] Howell, S. E., Babb, D. G., Landy, J. C., and Brady, M., "Multi-Year Sea Ice Conditions in the Northwest Passage: 1968–2020," *Atmosphere-Ocean*, 2022, pp. 1–15.

[84] Tang, C. C., Ross, C. K., Yao, T., Petrie, B., DeTracey, B. M., and Dunlap, E., "The circulation, water masses and sea-ice of Baffin Bay," *Progress in Oceanography*, Vol. 63, No. 4, 2004, pp. 183–228.

[85] Curry, B., Lee, C., Petrie, B., Moritz, R., and Kwok, R., "Multi-year volume, liquid freshwater, and sea ice transports through Davis Strait, 2004–10," *Journal of Physical Oceanography*, Vol. 44, No. 4, 2014, pp. 1244–1266.

[86] Hines, P., Barclay, D., Kessel, R., Deveau, T., Kusel, E., and Hamilton, J., "ASDA Final Modelling Report," Tech. rep., Geospectrum Technologies Inc., 2019.

[87] Hamilton, J., Chorney, N., Cole, A., Borys, P., and Martin, S., "Arctic Buoy Component Investigations," Tech. rep., JASCO Applied Sciences and JMH Consulting Design Inc. for Atlantic Research Centre, Defence Research and Development Canada, 2022.

[88] Wertz, J. R., Everett, D. F., and Puschell, J. J., *Space mission engineering: the new SMAD*, Microcosm Press, 2018.

[89] "Galileo Space Segment," https://www.esa.int/ESA_Multimedia/Images /2014/07/Galileo_constellation, 2021, Accessed 2023-02-06.

[90] "BeiDou Space Segment," https://gssc.esa.int/navipedia/index.php/ BeiDou_Space_Segment, 2021, Accessed 2023-02-06.

[91] Stassinopoulos, E. G., Xapsos, M. A., and Stauffer, C. A., "Forty-year" drift" and Change of the SAA," Tech. rep., 2015.

[92] Loh, K., "Walker-Delta Satellite Constellation for Earth Observation: SPE 510 Midterm Report," 2012.

[93] Su, Y., Liu, Y., Zhou, Y., Yuan, J., Cao, H., and Shi, J., "Broadband LEO satellite communications: Architectures and key technologies," *IEEE Wireless Communications*, Vol. 26, No. 2, 2019, pp. 55–61.

[94] Matricciani, E., "Geocentric spherical surfaces emulating the geostationary orbit at any latitude with zenith links," *Future Internet*, Vol. 12, No. 1, 2020, pp. 16.

[95] Abulgasem, S., Tubbal, F., Raad, R., Theoharis, P. I., Lu, S., and Iranmanesh, S., "Antenna designs for CubeSats: A review," *IEEE Access*, Vol. 9, 2021, pp. 45289–45324.

[96] "CubeSat VHF/UHF Transceiver," https://satsearch.co/products/data-patterns-cubesat-vhf-uhf-transceiver, 2009, Accessed 2023-02-20.

[97] "ISIS CubeSat VHF/UHF Transceiver," https://www.isispace.nl/product/isis-uhf-downlink-vhf-uplink-full-duplex-transceiver/, 2023, Accessed 2023-02-20.

[98] "CubeSat VHF/UHF Radio," http://www.aphelionorbitals.com/store/cubesat-uhfvhf-radio, 2018, Accessed 2023-02-20.

[99] "ISIS CubeSat VHF/UHF Antenna," https://www.isispace.nl/product/cubesat-antenna-system-1u-3u/, 2023, Accessed 2023-02-22.

[100] "NASA Small Spacecraft State of the Art," http://www.nasa.gov/smallsat-institute/sst-soa-2020, 2020, Accessed 2023-02-22.

[101] "VHF/UHF Ground Station," https://www.isispace.nl/wp-content/uploads/2016/02/ISIS-GSKit-DS-302_v1.2-VHFUHF-Ground-Station-DataSheet-for-website.pdf, 2019, Accessed 2023-02-24.

[102] "S-band Ground Station," https://www.isispace.nl/wp-content/uploads/2016/02/ISIS.GSKit_.DS_.303_v1.0-S-Band-Ground-Station-DataSheet-for-website.pdf, 2019, Accessed 2023-02-24.

[103] Wertz, J. R., Collins, J. T., Dawson, S., Koenigsmann, H. J., and Potter-veld, C. W., "Autonomous constellation maintenance," *Mission Design & Implementation of Satellite Constellations: Proceedings of an International Workshop, held in Toulouse, France, November 1997*, Springer, 1998, pp. 263–273.

[104] Kozhaya, S. E., Haidar-Ahmad, J. A., Abdallah, A. A., Kassas, Z. M., and Saab, S. S., "Comparison of neural network architectures for simultaneous tracking and navigation with LEO satellites," *Proceedings of the 34th International Technical Meeting of the Satellite Division of The Institute of Navigation (ION GNSS+ 2021)*, 2021, pp. 2507–2520.

[105] Auriol, A. and Tourain, C., "DORIS system: the new age," *Advances in space research*, Vol. 46, No. 12, 2010, pp. 1484–1496.

[106] "DORIS System," https://www.aviso.altimetry.fr/en/techniques/doris/doris-system/a-system-constantly-evolving.html, 2008, Accessed 2023-02-26.

[107] Arnold, D., Montenbruck, O., Hackel, S., and Sośnica, K., "Satellite laser ranging to low Earth orbiters: orbit and network validation," *Journal of geodesy*, Vol. 93, No. 11, 2019, pp. 2315–2334.

[108] Gramling, C. and Long, A., "Autonomous navigation using the TDRSS onboard navigation system (TONS)," *Advances in Space Research*, Vol. 16, No. 12, 1995, pp. 77–80.

[109] Hauschild, A. and Montenbruck, O., "Precise real-time navigation of LEO satellites using GNSS broadcast ephemerides," *NAVIGATION: Journal of the Institute of Navigation*, Vol. 68, No. 2, 2021, pp. 419–432.

[110] Mikhailov, N. and Vasil'ev, M., "Autonomous satellite orbit determination using spaceborne GNSS receivers," *Gyroscopy and Navigation*, Vol. 2, No. 1, 2011, pp. 1–9.

[111] Zhang, H., Wang, J., Yu, G., Zhong, J., and Lin, L., "An autonomous orbit determination method for MEO and LEO satellite," *7th International Symposium on Advanced Optical Manufacturing and Testing Technologies: Optical Test and Measurement Technology and Equipment*, Vol. 9282, SPIE, 2014, pp. 249–257.

[112] Montenbruck, O., Gill, E., Montenbruck, O., and Gill, E., "Introductory Astrodynamics," *Satellite Orbits: Models, Methods and Applications*, 2000, pp. 15–51.

[113] Vallado, D. A., *Fundamentals of astrodynamics and applications*, Vol. 12, Springer Science & Business Media, 2001.

[114] Widnall, S. and Peraire, J., "Lecture L17-Orbit Transfers and Interplanetary Trajectories," *Dynamics*, 2008.

[115] Brown, C. D., *Elements of spacecraft design*, Aiaa, 2002.

[116] Ha, J. C., "Mission Design & Implementation of Satellite Constellations," *Mission Design and Implementation of Satellite Constellations*, 1998.

[117] "ISIS On-Board Computer," https://www.isispace.nl/product/on-board-computer/, 2023, Accessed 2023-02-25.

[118] "GNSS Receiver," https://www.spacemanic.com/files/datasheet/datasheet-GPS-Celeste.pdf, 2023, Accessed 2023-02-25.

[119] "Integrated ADCS," https://satsearch_datasheet_krjdo3_arcsec_arcus-adcs.pdf, 2023, Accessed 2023-02-25.

[120] "CubeSat S-band Patch Antenna," https://www.isispace.nl/wp-content/uploads/2021/01/ISIS-SSPA-DSH-0001-S_Patch_Antenna_Datasheet-02_00.pdf, 2023.

[121] "CubeSat S-band Transmitter," https://www.aac-clyde.space/wp-content/uploads/2021/11/TX-2400-1.pdf, 2023.

[122] "CubeSat Solar Panels," https://www.spacemanic.com/files/datasheet/datasheet-SP-Ra.pdf, 2023.

[123] "CubeSat Batteries," https://www.isispace.nl/product/ieps-electrical-power-system/, 2023.

[124] Larson, W. J., Wertz, J. R., et al., *Space mission analysis and design*, Vol. 3, Springer, 1992.

[125] Accion Systems, "TILE Budget," 2022, Personal Correspondence.

[126] "Integrated ADCS," https://www.aac-clyde.space/wp-content/uploads/2021/11/iADCS200.pdf, 2023, Accessed 2023-02-28.

Appendices

A   Constellation Tables

Table A.1: Percent daily coverages of areas of strategic interest and selected ground stations for a Walker Delta constellation at an 83° inclination with 1 satellite per plane.

Walker Delta	Percent Daily Coverage (%)							
Number of Planes	Area A	Area B	Area C	Area D	Area E	Halifax	Winnipeg	Victoria
10	100	100	97.28	98.80	80.82	41.75	45.96	44.74
11	100	100	98.22	99.52	83.97	43.79	48.4	46.89
12	100	100	98.80	99.92	86.09	45.76	49.90	48.38
13	100	100	99.26	100	87.68	46.82	51.02	49.65
14	100	100	99.58	100	88.34	47.76	52.00	50.76
15	100	100	99.86	100	88.21	47.72	53.25	52.43
16	100	100	100	100	88.04	51.18	52.67	49.66
17	100	100	100	100	88.62	49.53	53.79	52.24
18	100	100	100	100	88.65	50.16	54.50	52.89
19	100	100	100	100	88.83	50.44	54.97	53.16
20	100	100	100	100	88.82	50.60	55.37	53.74

Table A.2: Percent daily coverages of areas of strategic interest and selected ground stations for a Walker Star constellation at an 83° inclination with 1 satellite per plane.

Walker Star	Percent Daily Coverage (%)							
Number of Planes	Area A	Area B	Area C	Area D	Area E	Halifax	Winnipeg	Victoria
10	99.73	97.73	91.34	93.43	74.69	36.29	40.54	38.74
11	99.95	98.86	92.94	95.02	76.86	36.65	41.64	39.81
12	100	99.23	94.23	96.33	78.22	38.14	42.36	40.47
13	100	99.46	95.30	97.37	78.83	39.35	43.28	41.06
14	100	99.65	96.17	98.20	79.34	39.93	44.03	41.60
15	100	99.8	96.93	98.82	79.60	40.00	44.28	42.38
16	100	99.89	97.57	99.29	79.91	40.57	44.90	43.27
17	100	99.97	98.08	99.52	80.13	41.62	44.37	42.25
18	100	100	98.57	99.64	80.46	40.94	45.77	43.56
19	100	100	98.97	99.74	80.69	41.21	45.83	43.88
20	100	100	99.30	99.82	80.88	41.36	45.91	44.08

Table A.3: Percent daily coverages of areas of strategic interest and selected ground stations for the selected Walker Delta constellation configuration at inclinations ranging from 80° to 89°.

Walker Delta 16 Planes	Percent Daily Coverage (%)							
Inclination (°)	Area A	Area B	Area C	Area D	Area E	Halifax	Winnipeg	Victoria
80	100	100	88.15	90.80	85.63	53.48	61.05	58.50
81	100	100	91.97	94.46	86.60	52.85	59.22	54.85
82	100	100	95.37	99.5	87.37	52.09	56.18	51.40
83	100	100	100	100	88.04	51.18	52.67	49.66
84	100	100	100	100	89.36	49.75	50.64	49.47
85	100	100	100	100	90.82	47.22	49.86	49.43
86	100	100	100	100	92.60	45.28	49.59	49.31
87	100	100	100	100	92.93	43.09	49.60	49.13
88	100	100	100	100	92.18	42.03	49.36	48.87
89	100	100	100	100	92.82	41.59	49.07	48.54

Table A.4: Percent daily coverages of areas of strategic interest and selected ground stations for the selected Walker Star constellation configuration at inclinations ranging from 80° to 89°.

Walker Star 20 Planes	Percent Daily Coverage (%)							
Inclination (°)	Area A	Area B	Area C	Area D	Area E	Halifax	Winnipeg	Victoria
80	100	99.99	85.88	88.13	77.35	42.95	47.94	45.85
81	100	100	88.98	92.42	78.41	42.31	47.08	45.00
82	100	100	93.73	98.78	79.66	41.90	46.50	44.34
83	100	100	99.30	99.82	80.88	41.36	45.91	44.08
84	100	100	99.74	99.88	82.19	40.98	45.52	43.63
85	100	100	99.79	99.91	83.77	40.72	45.27	43.40
86	100	100	99.83	99.94	85.50	40.45	44.96	43.15
87	100	100	99.87	99.96	87.49	40.45	44.63	42.58
88	100	100	99.90	99.97	89.81	40.32	44.50	42.38
89	100	100	99.91	99.98	92.77	40.23	44.09	42.44

Table A.5: Percent daily coverages of strategic areas of interest and ground stations for the selected Walker Delta constellation configurations.

Walker Delta 83° inclination	Percent Daily Coverage (%)							
Configuration	Area A	Area B	Area C	Area D	Area E	Halifax	Winnipeg	Victoria
1 Plane, 20 Satellites	100	100	98.28	100	76.44	38.70	43.90	42.18
2 Planes, 10 Satellites Each	100	100	100	100	100	44.58	51.78	49.43
4 Planes, 5 Satellites Each	83.94	96.59	99.56	99.13	100	63.28	62.99	62.79
5 Planes, 4 Satellites Each	67.84	78.94	85.87	84.32	98.12	50.51	62.82	58.54

Table A.6: Percent daily coverages of strategic areas of interest and ground stations for the selected Walker Star constellation configurations.

Walker Star 89° inclination	Percent Daily Coverage (%)							
Configuration	Area A	Area B	Area C	Area D	Area E	Halifax	Winnipeg	Victoria
1 Plane, 20 Satellites	100	100	100	100	92.68	37.94	42.68	41.18
2 Planes, 10 Satellites Each	100	100	100	100	100	69.98	78.70	75.86
4 Planes, 5 Satellites Each	80.27	87.77	89.87	89.62	87.83	63.08	63.06	62.99
5 Planes, 4 Satellites Each	64.72	71.25	74.83	74.03	78.22	51.24	53.25	52.48

Table A.7: Percent daily coverages of strategic areas of interest and ground stations for the selected Walker Star constellation with the altitude of the constellation ranging from 550 km to 600 km.

Walker Star	Percent Daily Coverage (%)							
Altitude	Area A	Area B	Area C	Area D	Area E	Halifax	Winnipeg	Victoria
550	100	100	100	100	99.77	66.16	74.37	71.83
560	100	100	100	100	99.84	66.88	75.24	72.93
570	100	100	100	100	99.91	67.58	76.02	73.61
580	100	100	100	100	99.96	68.41	76.91	74.27
590	100	100	100	100	99.99	69.05	77.77	75.10
600	100	100	100	100	100	69.98	78.70	75.86

Table A.8: Percent daily coverages of strategic areas of interest and ground stations for the selected Walker Star constellation with number of satellites per plane ranging from 8 to 10.

Walker Star	Percent Daily Coverage (%)							
Satellites per Plane	Area A	Area B	Area C	Area D	Area E	Halifax	Winnipeg	Victoria
8	100	100	99.93	99.97	98.50	64.08	72.24	69.75
9	100	100	100	100	99.81	67.56	75.92	73.58
10	100	100	100	100	100	69.98	78.70	75.86

B Link Margin

This appendix provides a representative first order calculation for link margins associated with this system. The calculations are conducted using values for the VHF uplink from the hydrophone to the satellite at the high end of the frequency range.

The first step in calculating the link margin is to calculated the effective isotropic radiated power (EIRP) of the transmitter in dB using

$$EIRP = P_t + G_t - L_l \tag{B.1}$$

where P_t is the transmission power (9.0 dB), G_t is the gain of the transmitter (0 dB), and L_l is the system line loss (3 dB) [88]. This gives an EIRP of The next step is to calculate the space loss of the signal. In order to do this, the maximum distance between the satellite and transmitter must first be determined with

$$d = \sqrt{2hR_e + h^2} \tag{B.2}$$

where h is the altitude of the satellite (600 km), and R_e is the radius of the Earth (6378 km) [88]. This results in a distance of 2830.8 km. Next, the wavelength of the signal must be determined using

$$\lambda = \frac{c}{f} \tag{B.3}$$

where c is the speed of light ($3 \times 10^8 \ \frac{m}{s}$) and f is the frequency of the signal (173.5 MHz) which gives a wavelength of 1.7 m. Now the space loss of the signal is calculated as

$$L_s = \left(\frac{4\pi d}{\lambda}\right)^2 \tag{B.4}$$

which results in a space loss of 146.3 dB [88]. Atmospheric attenuation of the signal is calculated as

$$L_a = \frac{zenith\ attenuation\ (dB)}{sin(\epsilon)} \tag{B.5}$$

where ϵ is the elevation angle ($1°$ since $\sin(0)$ is undefined) and the zenith attenuation is 0.02 dB [88]. This gives an atmospheric attenuation of 1.1 dB. The next step is to determine the signal to noise ratio $\frac{E_b}{N_o}$ using

$$\frac{E_b}{N_o} = EIRP + G_t - k_B - T_s - R - L_s - L_a \tag{B.6}$$

where k_B is the Boltzmann Constant (-228.6 dB), T_s is the system noise temperature (31.1 dB), and R is the data rate (39.8 dB) [124]. This results in an $\frac{E_b}{N_o}$ of 19.3 dB. Using a nominal bit error rate of 10^{-5} and the frequency shift keying modulation scheme commonly used by VHF receivers, the required $\frac{E_b}{N_o}$ is determined to be 13.3 dB. Nominal system loss values for polarization mismatch (0.3 dB), antenna pointing offset (0.2 dB), and system implementation (1 dB) are used for a first order link margin estimate calculated as

$$Link\ Margin = \frac{E_b}{N_o} - required\ \frac{E_b}{N_o} - system\ losses \tag{B.7}$$

which results in final link margin of 4.5 dB.

C Power Analysis

The first step in estimating the area of solar arrays required for the satellite is to establish the orbital period and maximum eclipse time of the satellite. The orbital period is calculated as

$$P = 2\pi\sqrt{\frac{r^3}{\mu}} \tag{C.1}$$

where r is the orbital radius of the satellite (6978 km) and μ is the Earth gravitational parameter (398,600 $\frac{\text{km}^3}{\text{s}^2}$). This gives an orbital period of 96.7 mins [88]. The maximum eclipse time of the satellite can be calculated with

$$T_e = \frac{2sin^{-1}\left(\frac{R_e}{r}\right)}{360°} \cdot P \tag{C.2}$$

where R_e is the radius of the Earth (6378 km) [88]. This results in a maximum eclipse time of 35.5 mins which when subtracted from the total orbit period leaves a daylight time (T_d) of 61.2 mins. The required solar array power for one orbit is expressed as

$$P_{sa} = \frac{\left(\frac{P_e T_e}{X_e} + \frac{P_d T_d}{X_d}\right)}{T_d} \tag{C.3}$$

where P_e is the peak power in eclipse (6.8 W), P_d is the average power in daylight (5.6 W), X_d is the transfer efficiency from arrays to batteries to subsystems (0.6), and X_e is the transfer efficiency from arrays to subsystems (0.8) [88]. The values for X_d and X_e correspond to efficiencies for the peak power tracking power regulation type which allows the solar panels to operate at maximum capacity independent from the charge level of the batteries [88]. This results in a required solar array power of 13.5 W. The next step is to determine the power output of the of the solar cells when normal to the sun

$$P_o = P_{in}\eta \tag{C.4}$$

where P_{in} is the average solar constant for a geocentric orbit ($1368 \frac{\text{W}}{\text{m}^2}$) and η is the efficiency of the solar cells (30%) [88]. This gives a power output of $410.4 \frac{\text{W}}{\text{m}^2}$. Calculating the beginning-of-life (BOL) power production of the solar array is done using

$$P_{BOL} = P_o I_d cos(\theta) \qquad \text{(C.5)}$$

where I_d is the inherent degradation of the solar array (0.72 nominal value) and θ is the angle between the sun and the solar arrays ($0°$ for first order approximation) [88]. This results in a BOL power output of $295.5 \frac{\text{W}}{\text{m}^2}$. Before determining the end-of-life (EOL) power, the lifetime degradation of the solar array must be calculated using

$$L_d = (1 - D)^L \qquad \text{(C.6)}$$

where D is the degradation per year (0.5% for multi-junction arrays), and L is the lifetime of the satellite (10 years) [88]. The lifetime degradation is calculated to be 0.95. This allows the EOL power to be calculated with

$$P_{EOL} = P_{BOL} L_d \qquad \text{(C.7)}$$

which gives an EOL power output of $281.0 \frac{\text{W}}{\text{m}^2}$ [88]. Finally, the required area of the solar array can be determined using

$$A_{sa} = \frac{P_{sa}}{P_{EOL}} \qquad \text{(C.8)}$$

which gives a solar array area of 479.5 cm^2. The required battery mass can be calculated by first determining the required battery capacity using

$$C_r = \frac{P_e T_e}{(DOD)Nn} \qquad \text{(C.9)}$$

where DOD is the depth of discharge (40% for Li-ion batteries), N is the number of batteries (1 to determine battery capacity), and n is the battery to load transfer efficiency (0.9 nominal) [88]. This gives a required battery capacity of 11.1 W·hr. The given values for energy storage and battery weight for the selected battery type are 22.5 W·hr and 0.184 kg [123]. This gives a battery energy density of $122.3 \frac{\text{W·hr}}{\text{kg}}$. This allows the battery mass to be calculated with

$$Battery\ Mass = \frac{C_r}{Energy\ Density} \qquad \text{(C.10)}$$

which gives a battery mass of 90.8 g [88].

D Thermal Calculations

The first step in the thermal analysis is to quantify the internal and external heat sources and corresponding maximum and minimum temperature limits. Solar heating can be calculated as

$$q_{Sun} = Q_{Sun} A_s \alpha_s \mu_i \tag{D.1}$$

where Q_{Sun} is the maximum solar flux density ($1419 \frac{W}{m^2}$), A_s is the area of the satellite exposed to the sun (0.14 m^2), α_s is the satellite absorptance (0.448 for a titanium alloy structure), and μ_i is the solar aspect coefficient (0.25 for a spherical satellite approximation) [124]. The solar heating is 12.4 W. Albedo heating can be calculated as

$$q_{albedo} = Q_{Sun} A_s \alpha_s a F_x \tag{D.2}$$

where a is the albedo coefficient of the Earth (0.30), and F_x is the view factor for a sphere calculated with

$$F_x = \frac{1}{2} \left(1 - \frac{\sqrt{h^2 + 2hR_e}}{h + R_e} \right) \tag{D.3}$$

where h is the altitude of the satellite (600 km), and R_e is the radius of the Earth (6378 km) [88]. This gives a view factor of 0.3. Using this value in equation (C.2) results in an albedo heating value of 8.0 W. Earth infrared (IR) heating is calculated with

$$q_{IR} = Q_{IR} A_s F_x \epsilon_{IR} \tag{D.4}$$

where Q_{IR} is the Earth IR flux density ($236 \frac{W}{m^2}$) and ϵ_{IR} is the IR emissivity of the spacecraft (0.148) [124]. This gives an Earth IR heating value of 1.5 W. Free molecular heating at 600 km altitude is negligible [88]. The daylight temperature of the satellite can be calculated using

$$T_{day} = \left(\frac{q_{Sun} + q_{albedo} + q_{IR} + q_{internal}}{\epsilon_{IR} A_s \sigma} \right)^{1/4} \tag{D.5}$$

where $q_{internal}$ is the internal heat of the satellite (5.6 W), and σ is the Stefan-Boltzmann constant (5.67×10^{-8} $\frac{\text{Wm}^2}{\text{K}^4}$) [88]. This results in a daylight temperature of 118.0°C [88]. The eclipse temperature can be calculated as

$$T_{eclipse} = \left(\frac{q_{IR} + q_{internal}}{\epsilon_{IR} A_s \sigma} \right)^{1/4} \tag{D.6}$$

which gives an eclipse temperature of 5.7°C [88]. The same calculations can be repeated using the revised anodized aluminum absorptivity and emissivity values of 0.25 and 0.33.